Precambrian Research 296 (2017) 148–167

Contents lists available at ScienceDirect

Precambrian Research

journal homepage: www.elsevier.com/locate/precamres

Initial breakup of supercontinent Rodinia as recorded by ca 860–840 Ma bimodal volcanism along the southeastern margin of the Yangtze Block, South China

Pu-Liang Lyu [a,b], Wu-Xian Li [a,*], Xuan-Ce Wang [c,d], Chong-Jin Pang [e], Jin-Xiong Cheng [a,b], Xian-Hua Li [f]

[a] State Key Laboratory of Isotope Geochemistry, Guangzhou Institute of Geochemistry, Chinese Academy of Sciences, Guangzhou 510640, China
[b] University of Chinese Academy of Sciences, Beijing 100049, China
[c] The Institute for Geoscience Research (TIGeR), Department of Applied Geology, Curtin University, GPO Box U1987, Perth, WA 6845, Australia
[d] School of Earth Science and Resources, Chang'an University, Shannxi, Xi'an 710054, China
[e] College of Earth Sciences, Guilin University of Technology, Guilin 541004, China
[f] State Key Laboratory of Lithospheric Evolution, Institute of Geology and Geophysics, Chinese Academy of Sciences, Beijing 100029, China

ARTICLE INFO

Article history:
Received 12 January 2017
Revised 7 April 2017
Accepted 26 April 2017
Available online 28 April 2017

Keywords:
Bimodal magmatism
Deep-Earth fluid cycling
Mantle hydration
Neoproterozoic
South China
Rodinia supercontinent

ABSTRACT

It is considered that mantle plumes play an important role in the breakup of supercontinents, but continental rifting and associated bimodal volcanism often predate mantle-plume magmatism and the major stage of supercontinent breakup. Therefore, the petrogenesis of those bimodal volcanic rocks is crucial for understanding the causal relationship between magmatism and supercontinent breakup. In this paper, new SIMS U–Pb zircon ages, Nd isotopic data, and whole-rock major and trace element data are reported for Huangshan and Meiling bimodal volcanic rocks that crop out along the southeastern margin of the Yangtze Block. The Huangshan and Meiling bimodal volcanic rocks were formed respectively at 860 ± 9 Ma and 840 ± 5 Ma, about 35 to 15 Mys earlier than the recorded Neoproterozoic plume event in South China. The Huangshan basalts have arc-like geochemical signatures with enrichment of water (pre-eruption magma water content of ~3.6%) and fluid-mobile elements, and depletion of high-field-strength elements (HFSE), as well as homogeneous Nd isotopic compositions ($\varepsilon_{Nd}(t)$ = +4.4 to +5.3). Although such geochemical characteristics suggest a hydrous asthenospheric mantle source for the Huangshan basalts, their incompatible trace elements plot within an intraplate tectonic setting, offset from true arc basalts. In contrast, the younger Meiling basalts have intraplate type (OIB-like) geochemical and homogeneous Nd isotopic compositions ($\varepsilon_{Nd}(t)$ = +4.3 to +4.7), implying a normal asthenospheric mantle source. Geochemical analyses indicate that the Huangshan basaltic rocks underwent olivine → olivine + amphibole + clinopyroxene + magnetite and then plagioclase fractional crystallization during magma ascent. Although mafic and felsic end-members have distinctive chemical compositions, the two end-members share similar Nd isotopic compositions. This implies that the felsic volcanic rocks were derived from basaltic rocks through fractional crystallization. The assemblage of fractional crystallization minerals may be amphibole-dominated and then plagioclase, coincident with fractioned mineral assemblage of the basaltic rocks. In contrast, Meiling felsic rocks have varied $\varepsilon_{Nd}(t)$ values that are correlated negatively with silica contents. Geochemical analyses indicate that the precursor magma underwent fractional crystallization of amphibole and plagioclase with minor titanite. This implies that Meiling felsic rocks were produced by partial melting of hydrous juvenile basaltic rocks, possibly ca 860 Ma underplated basaltic rocks, and then followed by variable crustal contamination. The petrogenesis of the 860–840 Ma bimodal volcanic rocks suggests that multi-stage rift-related anorogenic magmatism occurred before ca 825 Ma mantle-plume magmatism in South China. Wet upwelling, probably within or on top of the mantle transition zone, may have been the main cause of the hydration of the shallow asthenospheric mantle, which drove the mantle partial melting that generated these bimodal volcanic rocks. We conclude that mantle hydration was the trigger for early intracontinental rift-related magmatism, probably corresponding to the initial break-up of the Rodinia supercontinent.

* Corresponding author.
E-mail address: liwx@gig.ac.cn (W.-X. Li).

http://dx.doi.org/10.1016/j.precamres.2017.04.039
0301-9268/

1. Introduction

Episodic supercontinent assembly and breakup is now recognized as having profoundly influenced the course of the Earth's geological, climatic and biological evolution (e.g. Nance et al., 2014; Hoffman et al., 1998; Lindsay and Brasier, 2002; Condie, 2003, 1998, 2004; Hawkesworth et al., 2010). Although many researchers consider that mantle plumes play an important role in supercontinent breakup (Storey, 1995; Korenaga, 2004), early rifting, associated bimodal magmatism and some large igneous provinces (such as the ca 252 Ma Siberia Traps, which are much older than a major phase of continental rifting at ca 200 Ma), typically precede the major stage of supercontinent breakups (Lamotte et al., 2015; Li et al., 2010b). That bimodal magmatism may provide key information on the chemical and physical properties of the mantle, knowledge of which is crucial to an understanding of the driving force that initiated intracontinental rifting and subsequent supercontinent breakup (e.g., Wang et al., 2016).

The Supercontinent Rodinia is regarded as the assembly of the main continents during the Late Mesoproterozoic to Early Neoproterozoic (~1300–900 Ma, Li et al., 2008b; Condie, 2003; Evans, 2013). Initial dispersal of the Rodinia supercontinent occurred at ~ 750 Ma, when Greater India separated from NW Rodinia, and Australia-East Antarctica and South China broke away from Laurentia (Eyles and Januszczak, 2004; Li et al., 2008d). Prior to its breakup, multi-stage rifting events and associated anorogenic magmatism (~860–750 Ma) were widespread in the main blocks of the supercontinent (Paulsson and Andréasson, 2002; Cawood et al., 2015; Li et al., 2010b and references therein). In the South China Block, major magmatic events peaked at 850 Ma, 820–800 Ma and 780–750 Ma (Li et al., 2003b,c, 2005, 2008a,c,d, 2010b). Analyses of these magmatic events provide a rare chance to examine the cause that triggered the Neoproterozoic mantle plume (mantle upwelling) and final breakup of the Rodinia supercontinent.

Although Neoproterozoic rifting processes in the South China Block and other blocks of the Rodinia supercontinent have been much discussed (Moores, 1991; Li et al., 1995, 2008d; Karlstrom et al., 2000; Evans, 2009; Cawood et al., 2015), the driving force for early rifting and associated bimodal magmatism remains unclear (Li et al., 1999, 2002a, 2003a, 2005, 2003c, 2008a,c,d, 2010b). Two phases of bimodal volcanism, i.e., the Huangshan and Meiling events in northeastern Zhejiang Province, South China are identified by this study. Here, we present SIMS (secondary ion mass spectroscopy) U–Pb zircon ages, and whole-rock geochemical and Nd isotopic compositions of these bimodal volcanic rocks, with the aim to constrain the timing and mechanism of the initiation of Neoproterozoic rifting in South China and breakup of the Rodinia supercontinent.

2. Geological setting

The South China Block is widely considered to have formed by amalgamation of the Yangtze and Cathaysia blocks at ~1.0–0.9 Ga during the Sibao Orogeny (e.g. Chen and Jahn, 1998; Li et al., 2002b, 2008b, 2009a), although some researchers consider that the two blocks did not collide until ~800 Ma (e.g. Zhou and Lesher, 2002a; Zhou et al., 2002b, 2006; Zhao and Zhou, 2007a, b). The Yangtze and Cathaysia blocks are separated by the Jiangshan-Shaoxing Fault (JSF) in eastern South China (Fig 1 inset), although the southwestern extension of the JSF is not obvious because of post-Neoproterozoic sedimentary cover, and tectonic and magmatic modification. The oldest rocks in the Yangtze Block are in the Kongling Complex, which comprises Archean to Paleoproterozoic high-grade metamorphosed tonalites, trondhjemites and granodioritic gneisses, as well as amphibolites and metamorphosed supercrustal rocks (e.g. Qiu et al., 2000). Widespread marine clastic sedimentary rocks are interlayerd with mafic volcanic rocks along the southeastern margin of the Yangtze Block (Fig. 1 inset, shown as ~870–830 Ma volcanosedimentary successions). Traditionally, these were regarded to be metamorphosed Mesoproterozoic rocks, such as the Shuangxiwu Group in Zhejiang Province, the Shuangqiaoshan Group in Jiangxi Province, the Lengjiaxi Group in Hunan Province, the Sibao Group in Guangxi Province and the Fangjingshan Group in Guizhou Province (Shui, 1988; Li et al., 2010b references therein). However, U–Pb *in situ* dating of zircon from the sedimentary and volcanic rocks indicates that most of the rocks were formed at 900–830 Ma, during the Neoproterozoic (Wang et al., 2006, 2008b, 2013; Zhou et al., 2009; Li et al., 2010b; Zhang et al., 2013). Those rocks are locally unconformably overlain by Neoproterozoic (~825 Ma) volcanosedimentary rift successions (i.e., the Dengshan Group in northeastern Jiangxi Province and the Shangshu Group in northeastern Zhejiang Province) (Li et al., 2010b, 2010d).

The Shuangxiwu Group in Zhejiang Province is composed predominantly of coherent-volcanic and pyroclastic rocks interlayered with felsic tuffs, and tuffaceous sandstones and siltstones that are collectively strongly deformed and metamorphosed to lower greenschist facies (Zhu et al., 1996). The Shuangxiwu Group is subdivided into lower and upper sections. The lower section comprises basaltic volcanic rocks interlayered with siltstones, whereas the upper section comprises felsic pyroclastic rocks interlayered with basalts and rhyolites. The Shuangxiwu Group is overlain by Neoproterozoic volcanosedimentary rocks of the Heshangzhen Group (Gao et al., 2008). Basaltic and andesitic rocks of the lower section are dated at ~970 Ma, whereas andesitic and rhyolitic rocks from the middle and upper parts of Shuangxiwu Group are dated at 926 Ma and 891 Ma (Li et al., 2009a). The volcanic rocks have been interpreted to have formed along an active continental margin (Cheng, 1991; Ye et al., 2007; Li et al., 2009a).

We have identified two suites of bimodal volcanic rocks, previously interpreted to belong to the Shuangxiwu Group, in the Chencai region, near the JSF (Fig. 1). Based on differences between petrological associations, and degrees of metamorphism and deformation, we have assigned the names Huangshan and Meiling respectively to the southern and northern suites, and these are separated by a fault (Fig. 1).

The Huangshan suite is composed of basalts and rhyolites. Their true thickness is not known because of structural complications. Samples of the volcanic rocks were collected near Huangshan village in Zhuji County (Fig. 1). The basalts are dark grayish green in color, and are metamorphosed to upper greenschist facies; therefore, primary mineral assemblages have been modified. The metamorphic mineral assemblage is plagioclase (30–40%), chlorite (20–30%) and epidote (30–40%), as well as minor amphibole, biotite and the accessory minerals titanite, zircon, apatite and Fe–Ti oxides (opaque mineral). The rhyolites are light gray in color, with a phenocryst content of 5–10% comprising quartz (3–8%), plagioclase/K-feldspar (1–3%) and minor muscovite, in a matrix composed of quartz (30–40%), muscovite/sericite (30–40%) and feldspar (10–20%), as well as minor biotite and epidote and accessory zircon, apatite and Fe–Ti oxides. All rocks were strongly deformed by post-Neoproterozoic tectonic events.

The Meiling volcanic suite is dominantly composed of altered basalt and rhyolite. Samples of the volcanic suite were collected near Meiling village in Zhuji County (Fig. 1). The basalts are dark grayish green in color, are strongly deformed and metamorphosed

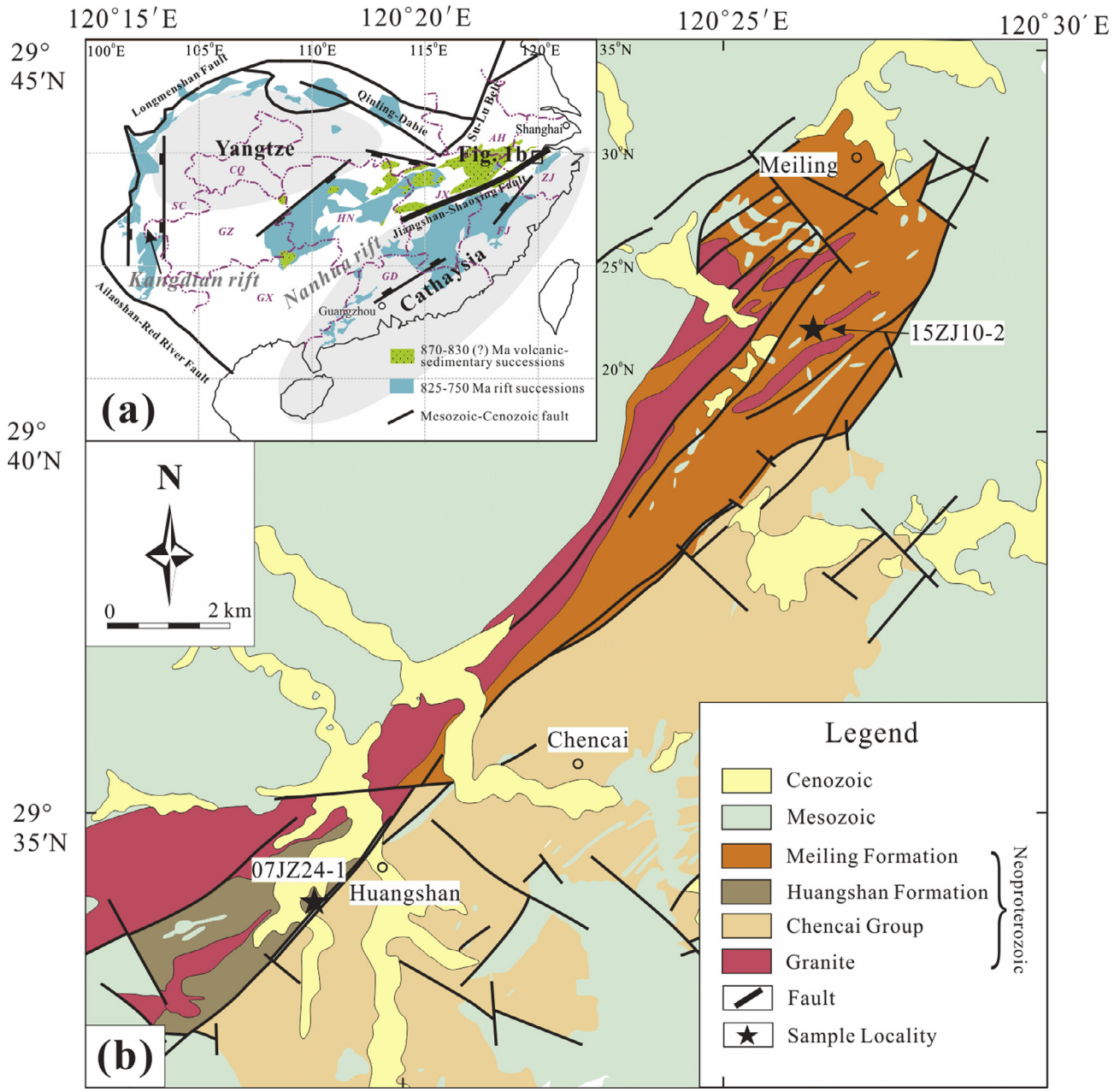

Fig. 1. (a) Distribution of mid-Neoproterozoic volcanic and sedimentary rocks and rift basins in the South China Block; modified after Li et al. (2010b). ZJ – Zhejiang Province; AH – Anhui Province; JX – Jiangxi Province; HN—Hunan Province; GX – Guangxi Province; FJ – Fujiang Province; GD – Guangdong Province; CQ – Chongqing city; SC – Sichuan Province. (b) Detailed geological map showing distribution of the Huangshan and Meiling volcanic rocks along with locations of samples used for geochronology.

to amphibolite facies. They are composed of amphibole (60–70%), plagioclase (20–30), Fe–Ti oxides (5–7%) and minor epidote (1–3%). The rhyolites are light gray in color, and comprise 15–40% phenocrysts. The phenocrysts are composed of plagioclase (50–60%), K-feldspar (10–20%) and quartz (20–30%), whereas the matrix is dominantly quartz, feldspar and muscovite/sericite with minor biotite and accessory minerals, such as zircon, apatite and Fe–Ti oxides. All rocks are strongly deformed and metamorphosed to greenschist facies.

Two rhyolite samples (07JZ24-1 from Huangshan, 29°33′21″N, 120°17′52″E; 15ZJ10-2 from Meiling, 29°40′55″N, 120°26′54″E) were collected for U–Pb zircon geochronology. Seventeen Huangshan volcanic rocks and fourteen less-altered Meiling volcanic rocks were collected for geochemical analyses.

3. Analytical methods

3.1. Major and trace element determinations

The collected samples were processed to remove weathered surfaces, and then pulverized to 200-mesh for elemental and isotopic analyses. Major element oxides were analyzed on fused glass beads using a Rigaku RIX 2000 X-ray fluorescence spectrometer at the State Key Laboratory of Isotope Geochemistry, Guangzhou Institute of Geochemistry, Chinese Academy of Sciences (SKLaBIG, GIGCAS). Calibration lines used in quantification were produced by bivariate regression of data from 36 reference materials encompassing a wide range of silicate compositions (Li et al., 2004). Analytical uncertainties are between 1% and 5%.

Trace elements were analyzed using an Agilent 7500a ICP-MS at SKLaBIG, GIGCAS. Analytical procedures were similar to those described by Li (1997) and Liu et al. (1996). A set of USGS and Chinese national rock standards, including BHVO-2, GSR-1, GSR-2, GSR-3, AGV-2, W-2 and SARM-4 was chosen for calibration. Analytical precision typically is better than 5%.

Nd isotope analyses were performed using a Micromass Isoprobe multi-collector mass spectrometer (MC-ICPMS) at SKLaBIG, GIGCAS. Analytical procedures are described by Li et al. (2004). The Nd fraction was separated by passing it through cation columns followed by HDEHP columns. Samples were taken up in 2% HNO_3, and the aqueous solutions were introduced into the MC-ICPMS using a Meinhard glass nebulizer with an uptake rate of 0.1 ml/min. The inlet system was cleaned for 5 min between analyses using high purity 5% HNO_3 followed by a blank solution of 2% HNO_3.The Isoprobe MC-ICPMS was operated in a static mode, and yielded $^{143}Nd/^{144}Nd = 0.512125 \pm 11$ (2σ) on 14 runs for the Shin Etsu JNdi-1 standard during this study. Measured $^{143}Nd/^{144}Nd$ ratios were normalized to $^{146}Nd/^{144}Nd = 0.7219$. The reported $^{143}Nd/^{144}Nd$ ratios are adjusted relative to the Shin Etsu JNdi-1 standard of 0.512115, corresponding to the La Jolla standard of 0.511860 (Tanaka et al., 2000).

3.2. Zircon U–Pb geochronology

Zircon crystals were separated using standard density and magnetic techniques. All zircon crystals were documented on transmitted and reflected light photomicrographs, and cathodoluminescence (CL) images, in order to examine internal structures. Measurements of U, Th and Pb concentrations were conducted using the Cameca IMS-1280 at Institute of Geology and Geophysics, Chinese Academy of Sciences and SKLaBIG, GIGCAS. Uranium-Th-Pb ratios were determined relative to the standard zircon TEMORA (Black et al., 2004) and Plešovice (Sláma et al., 2008), and absolute abundances were calibrated to the standard zircon 91500 (Wiedenbeck et al., 1995), using operating and data processing procedures similar to those described by Li et al. (2009b). Analyses of the Plešovice standard were interspersed with those of unknown grains. A long-term uncertainty of 1.5 percent (1 RSD) for $^{206}Pb/^{238}U$ measurements of the standard was propagated to the unknowns (Li et al., 2010a), despite the measured $^{206}Pb/^{238}U$ error during the course of this study generally being around 1% (1 RSD) or less. Measured compositions were corrected for common Pb using non-radiogenic ^{204}Pb. Corrections were sufficiently small to be insensitive to the choice of common Pb composition, and an average of present-day crustal composition (Stacey and Kramers, 1975) was used for the common Pb, assuming that the common Pb was largely surface contamination introduced during sample preparation. Uncertainties on individual analyses in the data tables are reported at the 1σ level. Mean ages for pooled U/Pb and Pb/Pb analyses are quoted with 2σ or 95% confidence intervals. Weighted mean U–Pb ages and Concordia plots were processed using the Isoplot/Ex v.3.0 program (Ludwig, 2003).

4. Analytical results

4.1. Zircon U–Pb geochronology

4.1.1. Huangshan rhyolites (07JZ24-1, 29°33′21″N; 120°17′52″E)

Zircon crystals separated from Sample 07JZ24-1 are euhedral and colorless, from 50 to 120 μm long, with length to width ratios ranging from 1:1 to 2:1. Most crystals show clear oscillatory zoning on cathodoluminescence (CL) images (Fig. 2a inset map). Fifteen analyses were conducted on 15 crystals during a single analytical session, giving a relatively wide range of U (28–1649 ppm) and Th (17–3137 ppm) concentrations (Table 1). Th/U ratios range from 0.19 to 1.91, implying a magmatic origin. Spots 8 and 14 produced respective $^{206}Pb/^{238}U$ ages of 557 and 741 Ma, which are younger than the age of the main population. This may be attributed to radiogenic Pb loss. The remaining thirteen analyses are concordant within analytical error, producing a concordant age of 860 ± 9 Ma (MSWD = 5.8; Fig. 2a), which is interpreted to be the eruption age of the rhyolites.

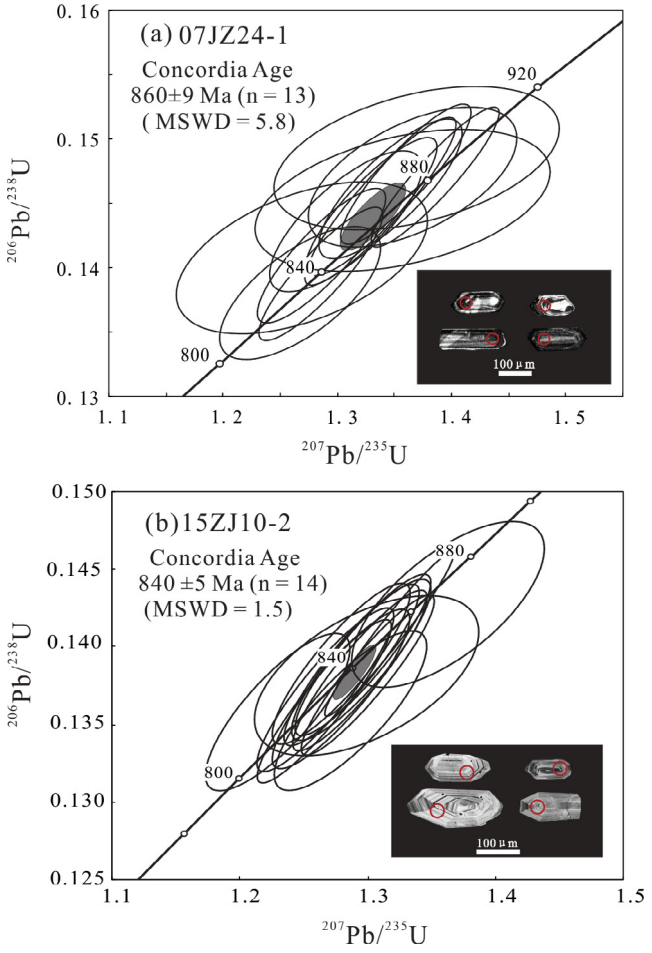

Fig. 2. SIMS zircon U–Pb concordia diagrams for the Huangshan (07JZ24-1) and Meiling (15ZJ10-2) rhyolitic rocks.

4.1.2. Meiling rhyolites (15ZJ10-2, 29°40′55″N; 120°26′54″E)

Zircon grains separated from Sample 15ZJ10-2 are euhedral, colorless, 80–150 μm long, with length to width ratios ranging from 1:1 to 3:1. Most zircon crystals show clear oscillatory zoning under CL images (Fig. 2b inset map). Fifteen analyses were conducted on 15 crystals. The analyses gave variable U (23–449 ppm) and Th abundances (12–806 ppm), with Th/U ratios mostly ranging from 0.52 to 1.79, similar to typical magmatic zircon (Table 1). Except for Spot 3, which is obviously younger than other analyses, fourteen analyses are concordant within analytical errors, producing a concordant age of 840 ± 5 Ma (MSWD = 1.5; Fig. 2b), which is interpreted to be the eruption age of the rhyolites.

4.2. Major and trace elements

Major and trace element data of Huangshan and Meiling bimodal volcanic rocks are listed in Table 2.

Table 1
SIMS zircon U-Pb isotopic results of rhyolites from Huangshan and Meiling bimodal volcanic suite.

Sample spot	U (ppm)	Th (ppm)	Th/U	f_{206}[a]	$^{207}Pb/^{235}U$	±1σ (%)	$^{206}Pb/^{238}U$	±1σ (%)	ρ[b]	$t_{207/206}$ (Ma)	±1σ	$t_{207/235}$ (Ma)	±1σ	$t_{206/238}$ (Ma)	±1σ	Discordance[c] (%)
07JZ24-1																
07JZ24-1-1	28	17	0.61	0.18	1.2703	3.50	0.1403	1.70	0.49	796	63	833	20	846	13	6.7
07JZ24-1-2	405	76	0.19	0.04	1.3470	1.88	0.1456	1.51	0.80	841	23	866	11	876	12	4.5
07JZ24-1-3	150	92	0.61	0.10	1.3083	2.06	0.1431	1.55	0.75	816	28	849	12	862	12	6.0
07JZ24-1-4	466	207	0.44	0.04	1.2867	1.70	0.1391	1.51	0.88	841	17	840	10	839	12	-0.2
07JZ24-1-5	926	1381	1.49	0.08	1.3603	1.70	0.1467	1.50	0.88	845	16	872	10	883	12	4.7
07JZ24-1-6	733	553	0.75	0.07	1.3857	1.63	0.1465	1.50	0.92	887	13	883	10	881	12	-0.7
07JZ24-1-7	304	211	0.69	1.88	1.3575	3.85	0.1447	1.54	0.40	870	71	871	23	871	13	0.2
07JZ24-1-8*	1649	2023	1.23	3.82	0.8266	2.15	0.0902	1.56	0.73	821	30	612	10	557	8	-33.6
07JZ24-1-9	635	663	1.04	0.20	1.3383	2.00	0.1446	1.82	0.91	841	17	863	12	871	15	3.8
07JZ24-1-10	530	946	1.78	0.26	1.2873	1.76	0.1405	1.50	0.85	821	19	840	10	847	12	3.4
07JZ24-1-11	546	502	0.92	0.21	1.3304	1.75	0.1442	1.50	0.86	835	18	859	10	868	12	4.3
07JZ24-1-12	113	48	0.43	2.86	1.3697	3.68	0.1480	1.52	0.41	842	68	876	22	889	13	6.0
07JZ24-1-13	779	965	1.24	0.64	1.3661	2.70	0.1465	1.50	0.56	857	46	875	16	881	12	3.0
07JZ24-1-14*	1641	3137	1.91	4.05	1.0528	2.99	0.1219	2.39	0.80	697	38	730	16	741	17	6.8
07JZ24-1-15	1083	1026	0.95	1.42	1.2688	2.24	0.1376	1.52	0.68	834	34	832	13	831	12	-0.4
15ZJ10-2																
15ZJ10-2-1	150	124	0.83	0.08	1.2938	1.71	0.1397	1.50	0.88	843	17	843	10	843	12	-0.1
15ZJ10-2-2	131	95	0.73	0.21	1.2783	1.71	0.1394	1.50	0.88	822	17	836	10	841	12	2.6
15ZJ10-2-3*	157	85	0.54	2.02	1.0663	2.2	0.1205	1.52	0.69	747	33	737	12	734	11	-1.9
15ZJ10-2-4	106	73	0.68	0.66	1.2980	2.75	0.1387	1.50	0.55	865	47	845	16	837	12	-3.4
15ZJ10-2-5	173	193	1.12	0.21	1.2781	1.71	0.1378	1.50	0.88	846	17	836	10	832	12	-1.7
15ZJ10-2-6	154	125	0.81	0.13	1.2659	1.72	0.1378	1.55	0.90	827	16	831	10	832	12	0.7
15ZJ10-2-7	151	175	1.16	0.06	1.2928	1.65	0.1390	1.50	0.91	852	14	843	9	839	12	-1.6
15ZJ10-2-8	210	370	1.76	0.14	1.2651	1.69	0.1370	1.55	0.92	836	14	830	10	828	12	-1.1
15ZJ10-2-9	136	118	0.87	0.38	1.2288	1.87	0.1364	1.50	0.80	786	23	814	11	824	12	5.2
15ZJ10-2-10	449	806	1.79	0.05	1.3155	1.55	0.1413	1.51	0.97	854	8	853	9	852	12	-0.2
15ZJ10-2-11	332	459	1.38	0.09	1.2989	1.63	0.1387	1.50	0.92	866	13	845	9	837	12	-3.5
15ZJ10-2-12	106	76	0.72	0.12	1.2855	1.88	0.1364	1.52	0.81	879	23	839	11	825	12	-6.5
15ZJ10-2-13	182	203	1.12	0.08	1.2951	1.67	0.1400	1.50	0.90	841	15	844	10	845	12	0.5
15ZJ10-2-14	162	138	0.85	0.13	1.2863	1.67	0.1394	1.51	0.90	836	15	840	10	841	12	0.7
15ZJ10-2-15	23	12	0.52	0.72	1.3614	2.25	0.1432	1.51	0.67	897	34	872	13	863	12	-4.1

Spots with asterisks are zircon grains that have suffered Pb loss. These analyses were not used in the calculation of the average age.
[a] f_{206} is the percentage of common ^{206}Pb in total ^{206}Pb assuming present-day Stacey-Kramers common Pb (Stacey and Kramers, 1975)
[b] ρ denotes error correlation between $^{207}Pb/^{235}U$ and $^{206}Pb/^{238}U$
[c] Discordance defined by percent deviation of $^{206}Pb/^{238}U$ age from $^{207}Pb/^{235}U$ age

4.2.1. Huangshan volcanic rocks

Huangshan volcanic rocks have a wide range of SiO_2 contents (49.7–79.1%, volatile-free), and a bimodal distribution in the plot of Zr/TiO_2 vs. SiO_2 (Fig. 3a, Winchester and Floyd, 1976) with a SiO_2 gap between ~55% and 70% (Fig. 4). Except for three high SiO_2 samples (SiO_2 > 53%), the other nine mafic samples plot into the basalt field. These Huangshan basaltic rocks have saturated to oversaturated silica with SiO_2 = 49.7–60.0%, low MgO (2.45–6.20%) and TiO_2 (0.63–1.35%), variable FeO^T (6.78–11.3%) and P_2O_5 (0.18–0.35%), and high Al_2O_3 (16.8–18.4%). All samples plot in the field of subalkaline basalt on the Zr/TiO_2 vs. SiO_2 diagram (Fig. 3a), and show a calc-alkaline trend on the TiO_2 vs. FeO^T diagram (Fig. 3b). As shown in Fig. 4, the contents of TiO_2, FeO^T, CaO and MgO decrease with increasing SiO_2 contents, whereas $Na_2O + K_2O$ increases with increasing SiO_2; P_2O_5 and Al_2O_3 show knee-like variations.

Chondrite-normalized REE patterns of Huangshan basaltic rocks are characterized by enriched LREE and fractionated HREE [$(La/Yb)_N$ = 3.71–7.64; $(Gd/Yb)_N$ = 1.46–2.17] (Subscript N = chondrite-normalized value; normalizing values are from Sun and McDonough, 1989), with dominantly positive Eu anomalies (Eu/Eu^* = 0.97–1.28), resembling to that of the E-MORB basalt (Fig. 5a). The primitive mantle-normalized trace-element distribution patterns of the basalts show obvious negative anomalies in high field strength elements (HFSE), i.e. Nb–Ta and Ti, but have slightly negative anomalies in Zr–Hf, similar to those of low-Ti Karoo continental flood basalts (CFBs, Fig. 5b).

The felsic rocks have SiO_2 contents of 69.4–79.1%. With the exception of two samples plotting into the rhyodacite field, the majority of the felsic rocks are classified as rhyolite on the diagram of Zr/TiO_2 vs. SiO_2 (Fig. 3a). These felsic rocks are characterized by high and variable Aluminum Saturation Index (A/CNK = $[Al_2O_3/(CaO + Na_2O + K_2O)]$ mol%) values (0.80–1.71, Table 2). On the chondrite-normalized diagram (Fig. 5e), the felsic rocks have slightly scoop-shaped patterns characterized by enriched LREE patterns with $(La/Yb)_N$ of 15.3–27.2 and flat HREE patterns with $(Gd/Yb)_N$ of 1.63 to 3.58, which resemble to the average of the Half Dome Granodiorite (Avg HD) formed by fractional crystallization of amphibole (Glazner et al., 2008). On the primitive mantle-normalized diagram (Fig. 5f), the felsic rocks have pronounced negative Nb–Ta and Ti anomalies. Contrarily, they have obviously positive Zr–Hf anomalies with dominant super-chondrite Zr/Sm ratios varying from 44 to 74.

4.2.2. The Meiling volcanic rocks

The Meiling volcanic rocks have a wide range of SiO_2 contents (46.5–74.2%), and a bimodal distribution in the plot of Zr/TiO_2 vs. SiO_2 with a narrow SiO_2 gap between 50% and 55% (Fig. 3a, Winchester and Floyd, 1976). All mafic rocks are basalts, whereas the majority of the felsic rocks plot in the fields of andesite and rhyolite-dacite (Fig. 3a). In contrast to the Huangshan basalts, the Meiling basalts are characterized by unsaturated silica (SiO_2 = 46.5–48.1%), high FeO^T (16.8–17.3%) and P_2O_5 (0.83–0.88%), but low Al_2O_3 (13.7–14.1%) and total alkali ($Na_2O + K_2O$ = 3.19–4.15%) contents (Fig. 4 and Table 2). They plot within the field of subalkaline basalts on the Zr/TiO_2 vs. SiO_2 diagram (Fig. 3a) and have a tholeiitic trend on the TiO_2 vs. FeO^T /MgO diagram (Fig. 3b).

Table 2
Major and trace element analyses of Huangshan and Meiling bimodal volcanic rocks.

Sample	07JZ25-1	07JZ25-2	07JZ25-3	15ZJ08-4	15ZJ08-5	15ZJ08-6	15ZJ08-7	15ZJ08-8	15ZJ08-11	07JZ31-4	07JZ31-5	07JZ31-7
Rock unit	B1	B1	B1	B1	B1	B1	B1	B1	B1	B2	B2	B2
SiO_2	52.1	52.5	49.7	51.1	60.0	53.1	51.7	54.6	50.8	48.1	46.6	47.0
TiO_2	0.90	1.23	1.26	1.17	0.63	1.08	1.35	1.32	1.05	3.30	3.19	3.29
Al_2O_3	17.9	18.0	16.8	18.1	17.8	17.5	18.4	18.1	18.4	14.1	14.0	14.0
FeO^T	10.7	10.6	11.3	9.68	6.78	9.26	9.25	8.76	10.2	16.9	16.8	17.0
MnO	0.16	0.14	0.17	0.17	0.18	0.18	0.19	0.17	0.19	0.22	0.24	0.24
MgO	4.39	4.57	6.20	5.48	2.45	5.02	4.45	3.55	4.83	5.29	5.66	5.40
CaO	7.85	7.40	9.44	7.10	5.15	7.48	9.42	6.98	8.89	7.28	8.44	8.59
Na_2O	3.42	3.20	3.06	2.27	4.34	1.90	3.39	3.23	3.89	0.57	1.20	2.33
K_2O	2.32	2.08	1.89	4.75	2.41	4.38	1.54	2.97	1.45	3.36	2.95	1.20
P_2O_5	0.20	0.30	0.23	0.20	0.28	0.18	0.30	0.35	0.29	0.88	0.87	0.88
Total[a]	99.94	100.02	100.05	100.02	100.02	100.08	99.99	100.03	99.99	100.00	99.95	99.93
LOI	2.30	2.60	3.04	6.17	1.55	4.46	2.48	2.18	1.61	8.01	8.01	4.27
Mg#[b]	46.2	47.5	53.6	54.3	41.9	53.2	50.2	46.0	49.8	39.7	41.4	40.0
A/CNK[c]												
Trace elements (ppm)												
Sc	27.3	23.7	29.5	25.8	11.6	25.6	22.0	23.4	26.3	23.8	40.0	32.2
V	259	202	248	221	95.4	221	235	201	260	302	275	314
Cr	38.7	17.9	40.6	22.9	9.95	29.6	33.9	26.1	24.9	72.7	95.7	108
Co	28.9	27.8	38.2	34.1	14.0	33.6	27.4	23.4	28.3	41.8	38.5	39.1
Ni	16.3	15.9	26.9	21.5	2.55	23.0	20.4	10.5	14.3	43.6	50.5	44.9
Ga	21.4	20.9	21.4	18.2	19.9	18.2	20.6	20.5	20.7	22.6	21.8	21.4
Ge	1.31	2.55	1.37	2.44	2.19	2.35	2.37	2.47	2.62	1.18	1.24	1.20
Rb	67.4	61.6	50.5	160	117	148	41.4	95.7	26.9	154	97.8	35.3
Sr	762	646	552	361	542	419	624	599	737	160	260	452
Y	14.7	20.2	14.6	16.7	16.5	17.7	15.0	24.0	14.5	46.6	49.4	52.2
Zr	49.9	117	79.1	73.2	102	69.8	80.0	126	70.2	222	218	234
Nb	3.84	6.06	4.72	4.29	4.79	4.40	4.25	6.92	3.03	9.75	10.4	9.99
Cs	5.40	5.27	3.59	19.0	4.43	13.6	3.50	6.05	0.931	11.9	9.02	7.52
Ba	388	422	401	289	357	462	337	374	458	1117	658	414
La	15.4	14.6	7.77	8.86	15.3	8.95	10.4	17.4	13.3	19.3	20.2	21.8
Ce	31.5	34.7	19.1	20.0	33.6	20.6	24.3	39.7	30.2	48.2	50.0	53.7
Pr	4.05	4.61	2.88	2.81	4.27	2.94	3.27	5.15	4.13	7.22	7.59	8.14
Nd	16.5	20.6	13.3	12.8	18.5	13.4	15.1	22.6	19.0	33.8	36.5	38.7
Sm	3.53	4.36	3.20	3.00	3.62	3.21	3.45	4.87	4.07	8.34	9.07	9.77
Eu	1.41	1.39	1.11	1.03	1.12	1.05	1.09	1.51	1.30	2.86	3.06	3.24
Gd	3.18	3.99	3.05	2.96	3.19	3.16	3.22	4.68	3.48	8.68	9.40	10.1
Tb	0.478	0.655	0.485	0.522	0.496	0.543	0.508	0.755	0.525	1.43	1.53	1.66
Dy	2.73	3.83	2.87	3.20	2.91	3.36	2.97	4.60	2.92	8.66	9.12	9.83
Ho	0.574	0.789	0.587	0.674	0.612	0.709	0.592	0.941	0.582	1.78	1.88	2.00
Er	1.47	2.11	1.48	1.80	1.68	1.91	1.56	2.53	1.53	4.91	5.13	5.44
Tm	0.224	0.296	0.221	0.259	0.249	0.278	0.212	0.356	0.211	0.713	0.734	0.781
Yb	1.44	1.83	1.34	1.68	1.62	1.73	1.32	2.27	1.32	4.51	4.60	4.90
Lu	0.224	0.295	0.201	0.266	0.264	0.278	0.210	0.355	0.205	0.685	0.698	0.746
Hf	1.43	3.29	1.99	2.34	2.92	2.25	2.35	3.66	2.11	5.26	5.17	5.45
Ta	0.209	0.321	0.302	0.336	0.375	0.318	0.290	0.492	0.164	0.604	0.581	0.606
Pb	17.9	8.68	11.5	12.9	12.6	16.0	10.5	17.9	6.85	18.4	16.3	14.7
Th	2.30	1.26	1.27	1.78	1.43	1.31	2.03	1.98	1.66	1.06	1.05	1.12
U	0.685	0.511	0.521	1.39	0.784	1.11	1.01	0.872	0.368	0.327	0.351	0.263

Sample	07JZ33-1	07JZ24-1	07JZ24-2	07JZ24-4	07JZ25-6	07JZ25-8	15ZJ08-1	15ZJ08-3	15ZJ08-10	07JZ31-2	07JZ33-3	07JZ33-5
Rock unit	B2	R1	R1	R1	R1	R1	R1	R1	R1	R2	R2	R2
SiO_2	46.5	77.3	77.3	77.8	79.1	77.0	75.3	72.1	69.4	71.5	73.1	69.7
TiO_2	3.13	0.17	0.16	0.14	0.20	0.22	0.21	0.36	0.36	0.42	0.39	0.53
Al_2O_3	13.7	13.8	14.2	14.4	12.6	13.4	13.8	14.5	14.1	14.9	16.1	15.3
FeO^T	17.3	1.62	1.79	1.02	1.31	1.55	2.39	2.86	3.03	3.35	2.78	3.60
MnO	0.29	0.02	0.02	0.01	0.03	0.02	0.13	0.10	0.11	0.07	0.05	0.09
MgO	5.72	0.53	0.52	0.32	0.22	0.39	0.57	0.82	1.49	0.90	0.71	1.49
CaO	9.40	0.29	0.23	0.17	0.22	0.24	0.27	1.70	3.80	1.94	1.98	1.34
Na_2O	2.51	3.28	2.96	2.71	4.04	3.20	4.45	4.18	3.98	5.38	3.72	4.79
K_2O	0.67	2.95	2.78	3.43	2.27	3.94	2.91	3.29	3.73	1.39	1.00	3.12
P_2O_5	0.83	0.01	0.01	0.01	0.04	0.04	0.05	0.09	0.09	0.11	0.10	0.13
Total[a]	100.05	99.97	99.97	100.01	100.03	100.00	100.08	100.00	100.09	99.96	99.93	100.09
LOI	1.32	1.55	1.88	0.96	0.89	2.40	0.79	0.87	1.16	1.82	0.93	1.31
Mg#[b]	41.0	40.6	37.9	39.6	25.9	34.4	33.2	37.6	50.8	36.0	35.0	46.4
A/CNK[c]		1.52	1.71	1.69	1.32	1.35	1.25	1.07	0.80	1.07	1.49	1.12
Trace elements (ppm)												
Sc	42.5	3.67	4.22	3.89	4.22	4.43	2.98	4.46	4.66	6.39	6.09	8.45
V	312	20.4	22.7	16.0	25.1	23.2	28.6	30.4	31.2	45.8	49.2	61.9
Cr	80.1	6.67	5.30	6.45	32.5	13.1	27.3	18.6	21.3	5.07	24.4	17.9
Co	42.6	3.22	2.84	2.18	2.68	2.78	2.71	5.12	5.58	4.82	4.91	7.63
Ni	48.1	6.65	6.03	3.57	5.63	4.37	4.52	4.65	5.52	3.95	4.45	6.80

(*continued on next page*)

Table 2 (*continued*)

Sample	07JZ33-1	07JZ24-1	07JZ24-2	07JZ24-4	07JZ25-6	07JZ25-8	15ZJ08-1	15ZJ08-3	15ZJ08-10	07JZ31-2	07JZ33-3	07JZ33-5
Rock unit	B2	R1	R1	R1	R1	R1	R1	R1	R1	R2	R2	R2
Ga	21.3	21.1	23.4	22.0	21.1	21.6	14.8	16.1	16.7	22.1	22.2	22.2
Ge	1.18	1.72	1.62	1.64	1.67	1.64	1.14	1.45	1.47	1.57	1.60	1.56
Rb	10.8	44.2	39.1	58.9	47.1	70.1	43.3	65.4	82.5	26.4	23.4	52.6
Sr	357	396	123	104	65.3	93.8	67.1	251	184	419	426	234
Y	50.9	4.48	7.30	5.80	9.21	8.48	6.88	14.3	12.8	13.9	15.5	15.9
Zr	223	104	84.1	118	139	145	120	231	213	199	181	185
Nb	9.60	2.36	6.35	6.31	7.19	6.61	6.00	8.46	8.63	9.47	8.88	8.48
Cs	1.02	3.07	2.17	1.87	3.30	2.42	1.85	1.87	3.05	1.46	0.972	0.613
Ba	290	128	1527	780	265	559	675	992	1014	798	986	1015
La	21.4	7.39	23.7	21.1	22.5	28.4	19.3	31.5	33.7	28.7	25.0	24.6
Ce	52.4	12.3	39.3	38.6	41.8	53.4	35.9	56.8	59.8	52.9	47.7	44.1
Pr	7.97	2.25	4.04	4.38	4.69	6.00	4.04	5.96	6.53	5.91	5.59	5.59
Nd	37.7	8.94	12.7	14.4	16.0	20.7	14.2	20.5	22.1	20.5	19.8	20.7
Sm	9.48	1.85	1.81	2.23	2.65	3.31	2.26	3.10	3.29	3.50	3.45	3.69
Eu	3.24	0.538	0.515	0.582	0.476	0.521	0.354	0.759	0.698	0.797	0.854	0.892
Gd	10.0	1.33	1.52	1.71	2.06	2.56	1.92	2.91	2.95	2.85	2.96	3.19
Tb	1.61	0.186	0.208	0.224	0.298	0.332	0.245	0.408	0.405	0.417	0.457	0.471
Dy	9.59	0.911	1.18	1.16	1.64	1.65	1.36	2.40	2.36	2.39	2.65	2.73
Ho	1.95	0.183	0.263	0.232	0.342	0.326	0.276	0.514	0.482	0.502	0.560	0.580
Er	5.37	0.340	0.663	0.531	0.859	0.766	0.743	1.50	1.31	1.40	1.57	1.57
Tm	0.766	0.051	0.111	0.085	0.141	0.120	0.111	0.223	0.193	0.226	0.254	0.246
Yb	4.81	0.308	0.769	0.572	0.917	0.749	0.745	1.48	1.24	1.56	1.67	1.66
Lu	0.728	0.047	0.122	0.096	0.148	0.124	0.126	0.250	0.207	0.254	0.278	0.271
Hf	5.25	2.78	2.33	3.53	3.91	4.15	4.19	6.59	6.05	4.93	4.51	4.48
Ta	0.602	0.142	0.510	0.504	0.673	0.401	0.566	0.754	0.669	0.681	0.637	0.580
Pb	10.5	13.0	13.2	11.9	9.56	10.5	6.09	12.5	14.2	25.9	15.3	15.3
Th	1.09	1.53	3.68	9.03	9.20	13.2	9.73	6.00	6.50	7.28	5.17	6.39
U	0.256	0.341	0.373	0.804	1.13	0.755	1.09	1.41	1.13	1.65	1.39	1.43

Sample	07JZ35-2	07JZ35-3	15ZJ09-1	15ZJ09-2	15ZJ09-3	15ZJ10-1	15ZJ10-2	15ZJ10-3	15ZJ10-4
Rock unit	R2	R2	R2	R2	R2	R2	R2	R2	R2
SiO_2	73.0	74.2	63.8	62.3	61.2	62.6	74.1	56.2	57.5
TiO_2	0.44	0.38	0.83	0.73	0.75	0.73	0.24	2.00	1.86
Al_2O_3	14.6	14.5	17.3	18.5	18.8	16.9	14.0	16.3	16.7
FeO^T	2.20	1.61	5.07	4.64	4.94	5.62	2.02	8.58	8.18
MnO	0.06	0.06	0.14	0.16	0.17	0.14	0.11	0.20	0.20
MgO	0.68	0.67	1.95	1.71	1.74	2.45	0.53	3.08	2.86
CaO	3.34	1.78	3.89	3.69	3.32	4.51	1.39	7.14	6.30
Na_2O	1.23	3.41	3.13	5.17	4.78	3.43	6.08	3.75	4.42
K_2O	4.32	3.29	3.68	2.77	3.93	3.49	1.45	2.07	1.47
P_2O_5	0.08	0.07	0.25	0.34	0.36	0.17	0.07	0.61	0.54
Total[a]	99.95	99.97	100.04	100.01	99.99	100.04	99.99	99.93	100.03
LOI	4.57	2.55	4.67	1.80	2.29	4.33	1.40	0.84	0.95
Mg#[b]	39.3	46.6	44.7	43.6	42.5	47.8	35.7	41.8	41.1
A/CNK[c]	1.15	1.17	1.07	1.01	1.04	0.96	0.99	0.76	0.82
Trace elements (ppm)									
Sc	5.60	5.65	13.0	10.6	10.8	15.0	3.10	20.7	18.5
V	23.9	20.4	86.0	54.9	64.2	120	17.9	184	161
Cr	10.1	6.97	13.9	11.9	6.13	13.5	16.1	6.76	13.1
Co	2.77	2.33	11.7	6.58	7.42	13.9	2.49	19.8	20.6
Ni	4.23	3.45	5.53	2.21	2.80	8.40	2.47	5.53	8.99
Ga	22.0	22.3	18.4	20.2	20.4	18.7	13.3	18.9	19.2
Ge	1.57	1.60	2.10	2.20	2.02	1.91	1.17	2.47	2.33
Rb	127	83.9	116	60.4	72.9	57.2	27.1	40.8	27.6
Sr	139	210	203	423	314	437	271	595	551
Y	26.0	21.4	19.3	21.0	18.5	16.1	9.24	19.8	19.8
Zr	339	301	250	173	167	125	146	106	88.6
Nb	16.7	13.4	8.93	6.65	6.60	7.07	5.99	6.07	7.33
Cs	5.22	1.63	9.09	1.24	1.68	1.46	0.421	1.43	1.11
Ba	846	1080	604	1194	1280	930	606	574	439
La	42.4	38.5	29.0	25.8	24.3	22.0	20.0	18.4	19.0
Ce	82.2	74.3	59.1	55.7	52.8	43.5	35.7	41.3	41.9
Pr	9.46	8.45	7.67	6.87	6.54	5.38	3.64	5.39	5.54
Nd	33.3	29.7	31.7	28.5	27.0	21.2	12.3	23.4	24.2
Sm	5.74	5.05	5.95	5.48	5.49	3.91	1.91	4.76	4.91
Eu	0.992	1.07	1.42	1.55	1.48	1.01	0.453	1.40	1.42
Gd	5.06	4.25	4.87	4.67	4.46	3.46	1.75	4.37	4.45
Tb	0.768	0.639	0.691	0.692	0.662	0.519	0.249	0.667	0.681
Dy	4.42	3.67	3.90	3.92	3.72	3.05	1.51	3.83	3.85
Ho	0.920	0.759	0.784	0.808	0.750	0.619	0.332	0.781	0.781
Er	2.68	2.27	2.06	2.19	2.13	1.73	1.01	2.07	2.06
Tm	0.441	0.371	0.304	0.323	0.308	0.250	0.164	0.287	0.282
Yb	3.01	2.48	1.94	2.06	2.00	1.61	1.17	1.78	1.73

Table 2 (*continued*)

Sample	07JZ35-2	07JZ35-3	15ZJ09-1	15ZJ09-2	15ZJ09-3	15ZJ10-1	15ZJ10-2	15ZJ10-3	15ZJ10-4
Rock unit	R2	R2	R2	R2	R2	R2	R2	R2	R2
Lu	0.474	0.396	0.313	0.333	0.319	0.258	0.205	0.282	0.274
Hf	8.69	7.56	6.49	4.78	4.25	4.09	4.61	3.40	2.94
Ta	1.30	1.07	0.544	0.426	0.400	0.550	0.674	0.514	0.559
Pb	14.6	18.1	5.90	8.62	8.03	9.93	5.93	6.98	6.59
Th	16.8	13.1	4.46	4.43	4.15	4.44	5.81	2.93	2.87
U	2.00	2.68	1.32	1.26	1.14	1.38	1.27	0.983	0.893

[a] Including loss-on-ignition (LOI).
[b] Mg# = 100*Mg/(Mg+Fe^{2+}), assuming Fe^{2+}/Fe^{total} = 0.9.
[c] A/CNK = [Al_2O_3/(CaO + Na_2O + K_2O)] mol%. B1-Huangshan basalts; B2-Meiling basalts; R1-Huangshan rhyolites; R2-Meiling rhyolites.

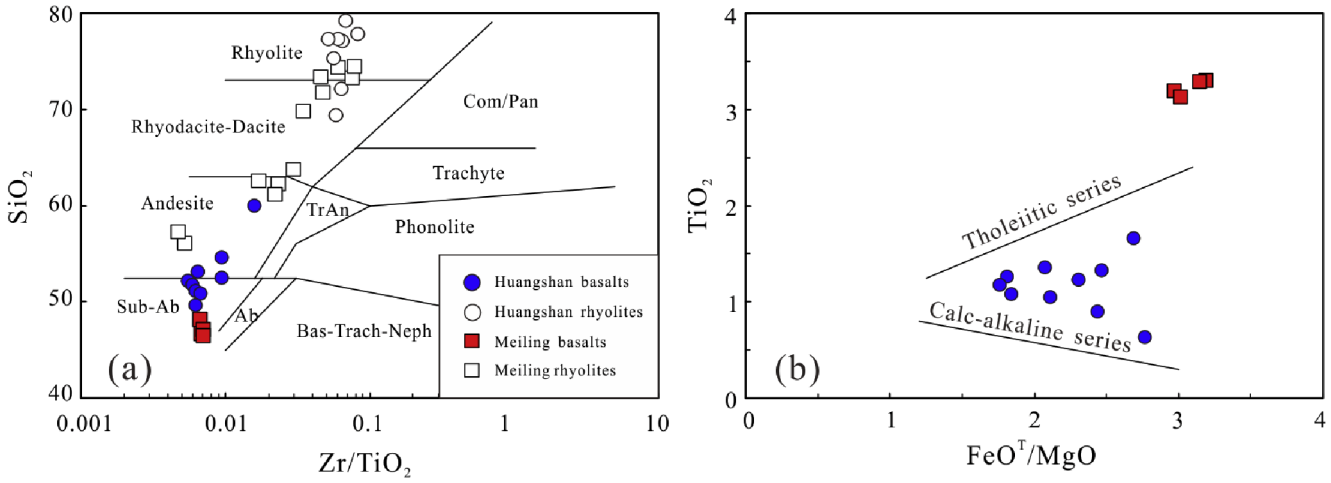

Fig. 3. Rock classification diagrams of (a) Zr/TiO_2 – SiO_2 diagram after Winchester and Floyd (1977). Sub-Ab – Sub Alkaline basalt; Ab – Alkaline basalt, (b) TiO_2 – FeO^T/MgO diagram after Miyashiro (1974).

The basaltic rocks are characterized by enriched LREE, less-fractionated HREE patterns [$(La/Yb)_N$ = 3.08–3.20; $(Gd/Yb)_N$ = 1.59–1.73], and insignificant Eu anomalies (Eu/Eu^* = 0.99–1.03) (Fig. 5c). On the primitive mantle-normalized trace element diagram (Fig. 5d), the basalts are enriched in incompatible trace elements, and depleted in Th, U, Nb and Ta relatively to neighboring elements.

With the exception of two rhyolite samples, the majority of the felsic rocks plot into the andesite and rhyolite-dacite field on the diagram of Zr/TiO_2 vs. SiO_2 (Fig. 3a). On the chondrite-normalized diagram, these felsic rocks show enrichment of LREE patterns [$(La/Yb)_N$ = 7.41–13.2], with negative Eu anomalies (Eu/Eu^* = 0.56–0.94) (Fig. 5g). These felsic rocks have scoop-shaped patterns that are characterized by enriched LREE and flat HREE patterns with $(Gd/Yb)_N$ of 1.24 to 2.13, which are similar to that of Avg HD formed by fractional crystallization of amphibole (Glazner et al., 2008). The high-silica felsic samples are similar to the Fish Canyon Tuff (FCT) glass formed by fractional crystallization of amphibole plus minor titanite (Bachmann et al., 2005; Glazner et al., 2008). On the primitive mantle-normalized diagram, the felsic rocks have prominent negative Nb, Ta and Ti anomalies with variable Zr–Hf anomalies (Fig. 5h).

4.3. Nd isotopic compositions

Neodymium (Nd) isotopic data of the Huangshan and Meiling samples are presented in Table 3. The Huangshan basaltic rocks have relatively high $^{147}Sm/^{144}Nd$ (0.1185–0.1456) and $^{143}Nd/^{144}Nd$ ratios (0.512466–0.512608), corresponding to $\varepsilon_{Nd}(t)$ values of +4.45 to +5.32. The Huangshan felsic rocks have similar Sm-Nd isotopic composition ($^{143}Nd/^{144}Nd$ = 0.512296–0.512347; $\varepsilon_{Nd}(t)$ = +4.92–+5.40) to their basaltic counterparts. The Nd model ages (T_{DM}) of the Huangshan felsic rocks are 1.05–1.08 Ga.

The Meiling basaltic rocks have $^{147}Sm/^{144}Nd$ ratios of 0.1503–0.1526 and $^{143}Nd/^{144}Nd$ ratios of 0.512611–0.512624, corresponding to $\varepsilon_{Nd}(t)$ values of +4.28 to +4.72. The felsic rocks have a relatively large range of $^{147}Sm/^{144}Nd$ (0.0941–0.1227) and $^{143}Nd/^{144}Nd$ ratios (0.512194–0.512501), corresponding to $\varepsilon_{Nd}(t)$ values of +1.30 to +5.27, with Nd model ages (T_{DM}) of 1.09–1.33 Ga.

5. Petrogenesis

5.1. Effects of alteration on whole-rock compositions

Mobile element contents may have been modified by deformation and greenschist-facies metamorphism. Therefore, the effects of alteration on whole-rock major and trace elements of the studied rocks need to be evaluated before discussing their geochemical characteristics and petrogenesis. Plots of LOI versus selected major and trace elements can be used to test the mobility of these elements during alteration (Wang et al., 2010). As shown in Fig. 6, the positive correlation of K_2O with LOI for the mafic and felsic rocks probably reflects K alteration (e.g., Crawford and Hilyard, 1990). The negative correlation of Na_2O with LOI suggests that Na has been leached from the rocks, and was probably caused by plagioclase alteration (Wang et al., 2010). The other major elements show in total no correlation with LOI, suggesting that they are immobile. All trace elements, except for Rb and Sr, show no obvious correlation with LOI, suggesting that they are immobile, whereas Rb and Sr are probably mobile. Bivariate plots of Zr against selected trace elements (figures not

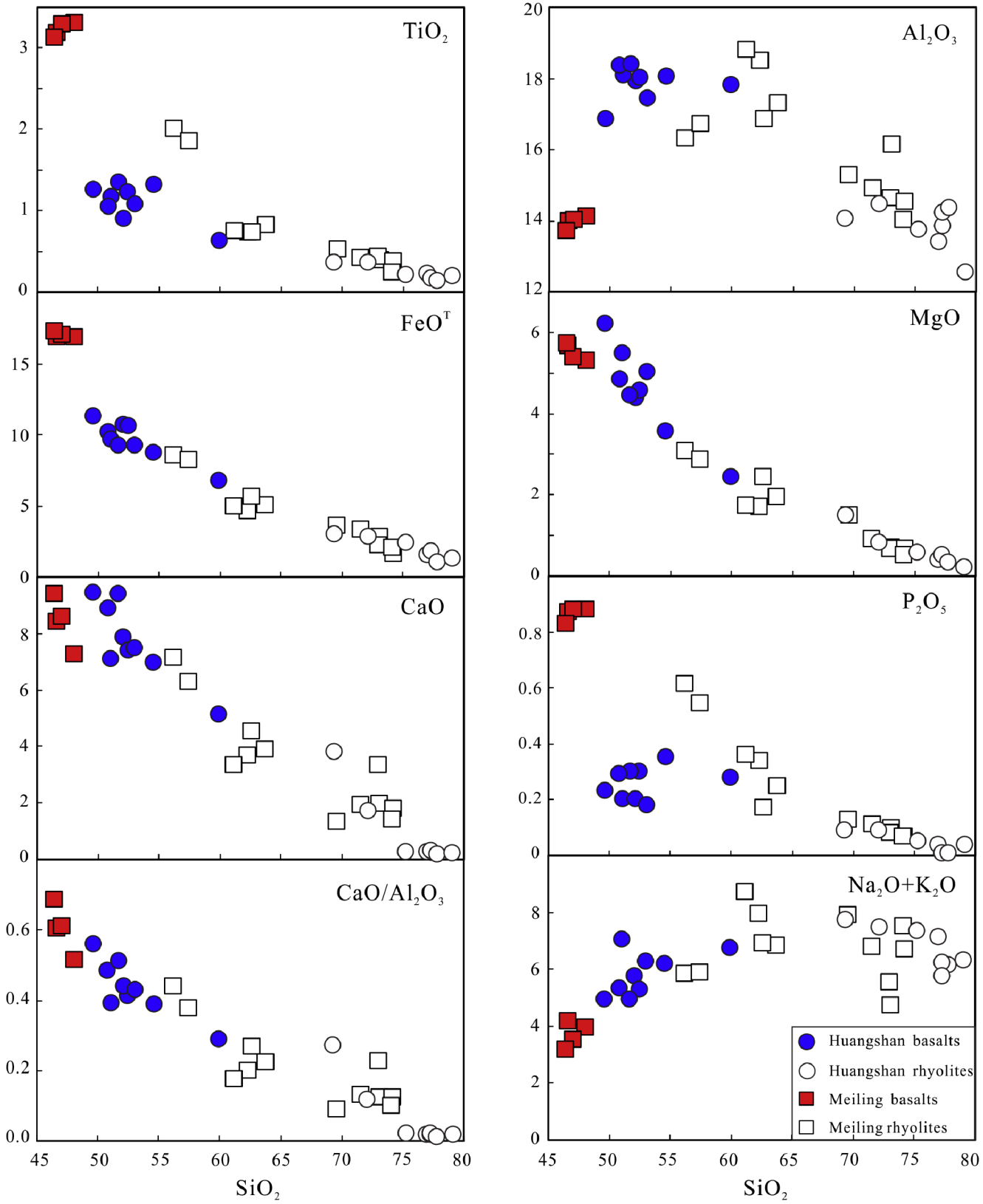

Fig. 4. Binary variation diagrams of the Huangshan and Meiling basalts showing major elements and ratios versus SiO_2 variations.

show) can also be used to evaluate the mobility of major and trace elements during alteration (Polat et al., 2002; Wang et al., 2008a, 2010). High field strength elements (HFSE, such as Nb and Zr), rare earth elements (REE), Y and U are all well-correlated with Zr, suggesting that they were essentially immobile during alteration. In contrast, the lack of correlation between Zr and fluid-mobile elements (e.g., Rb, Sr, Ba and K) suggests mobility of these elements during post-magmatic alteration. In conclusion therefore, only the immobile elements are used here in the following discussions.

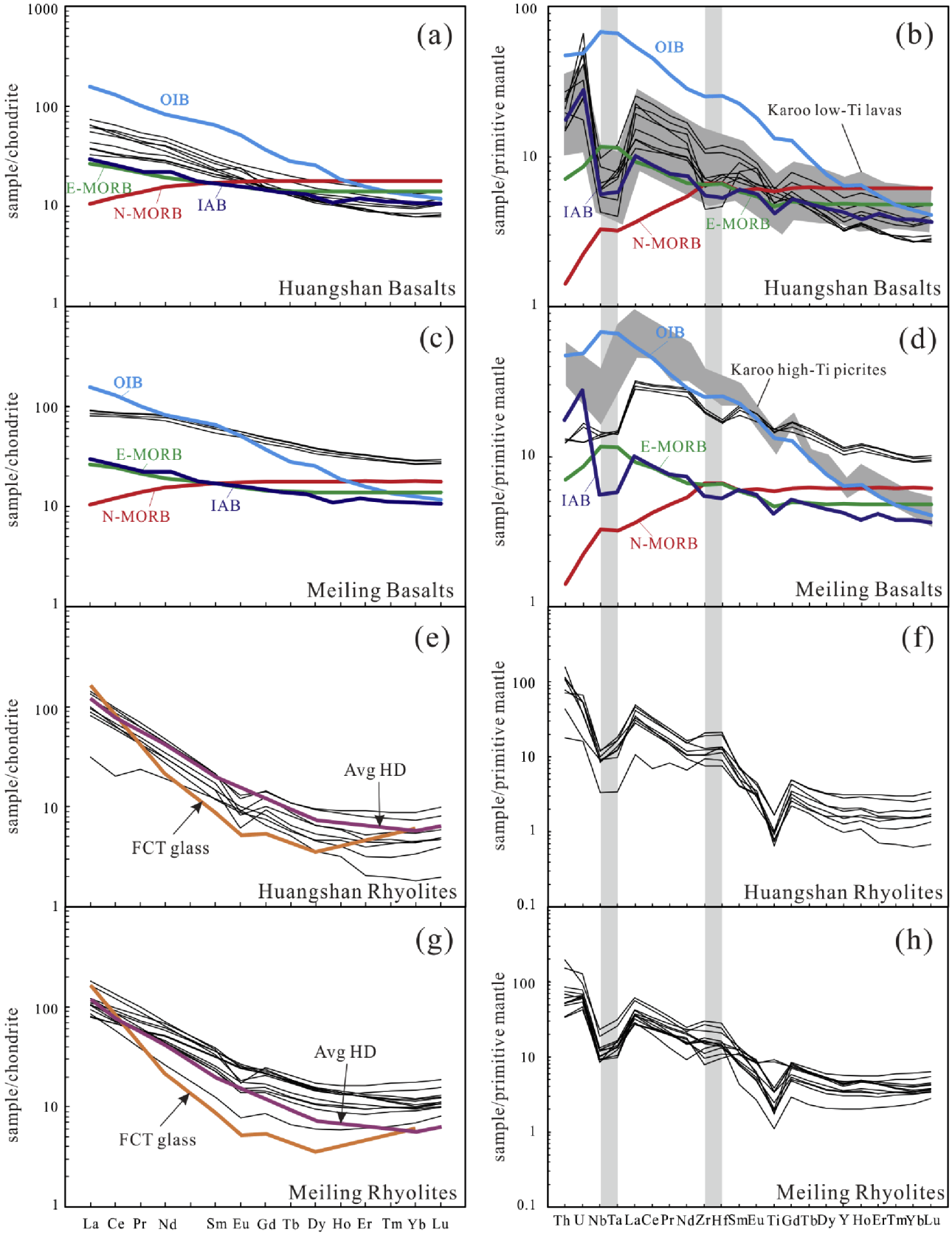

Fig. 5. Chondrite-normalized REE patterns (a, c, e, g), and primitive mantle-normalized incompatible element distribution diagrams (b, d, f, h) for the Huangshan and Meiling bimodal volcanic rocks. The chondrite normalized values are from Sun and McDonough (1989). The data of OIB, E-MORB, N-MORB are from Sun and McDonough (1989), the Karoo high-Ti picrites and Karoo low-Ti basalts are from Jourdan et al. (2007), and the island arc basalt (IAB) is from Kelemen et al. (2003).

Table 3
Results of Nd isotopic compositions for Huangshan and Meiling bimodal volcanic rocks.

	Sm (ppm)	Nd (ppm)	$^{147}Sm/^{144}Nd$	$^{143}Nd/^{144}Nd$	$2\sigma_m$	$\varepsilon_{Nd}(t)$	T_{DM} (Ga)
Huangshan Basalts							
07JZ25-1	3.53	16.5	0.1293	0.512484	0.000007	4.45	
07JZ25-2	4.36	20.1	0.1309	0.512505	0.000005	4.70	
07JZ25-3	3.20	13.3	0.1456	0.512608	0.000004	5.09	
15ZJ08-5	3.62	18.5	0.1185	0.512466	0.000008	5.32	
15ZJ08-7	3.45	15.1	0.1381	0.512569	0.000006	5.15	
15ZJ08-11	4.07	19.0	0.1292	0.512491	0.000005	4.38	
Meiling Basalts							
07JZ31-5	9.07	36.5	0.1503	0.512624	0.000004	4.72	
07JZ31-7	9.77	38.7	0.1526	0.512618	0.000004	4.34	
07JZ33-1	9.48	37.7	0.1520	0.512611	0.000004	4.28	
Huangshan Rhyolites							
07JZ25-6	2.65	16.0	0.1003	0.512347	0.000005	4.99	1.08
07JZ25-8	3.31	20.7	0.0967	0.512323	0.000005	4.92	1.08
15ZJ08-1	2.26	14.2	0.0963	0.512345	0.000004	5.40	1.05
15ZJ08-3	3.10	20.5	0.0915	0.512296	0.000005	4.99	1.07
Meiling Rhyolites							
07JZ33-5	3.69	20.7	0.1077	0.512355	0.000006	4.03	1.14
07JZ35-2	5.74	33.3	0.1043	0.512196	0.000005	1.30	1.33
07JZ35-3	5.05	29.7	0.1029	0.512194	0.000005	1.39	1.31
15ZJ09-2	5.48	28.5	0.1163	0.512410	0.000005	4.18	1.16
15ZJ10-2	1.91	12.3	0.0941	0.512240	0.000005	3.24	1.16
15ZJ10-4	4.91	24.2	0.1227	0.512501	0.000005	5.27	1.09

$\varepsilon Nd(t) = [(^{143}Nd/^{144}Nd)_{Sample}(T)/(^{143}Nd/^{144}Nd)_{CHUR}(T) - 1] * 10^4$.
$(^{143}Nd/^{144}Nd)_{Sample}(t) = (^{143}Nd/^{144}Nd)_{Sample} - (^{147}Sm/^{144}Nd)_{Sample} * (e^{\lambda T} - 1)$.
$(^{143}Nd/^{144}Nd)_{CHUR}(t) = 0.512638 - 0.1967 * (e^{\lambda T} - 1)$.
$T_{DM} = 1/\lambda_{Sm} \times \ln\{[(^{143}Nd/^{144}Nd)_S - 0.51315]/[(^{147}Sm/^{144}Nd)_S - 0.2137]\}$
$\lambda_{Sm\text{-}Nd} = 0.00654\ Ga^{-1}$ (Jacobsen and Wasserburg, 1984).

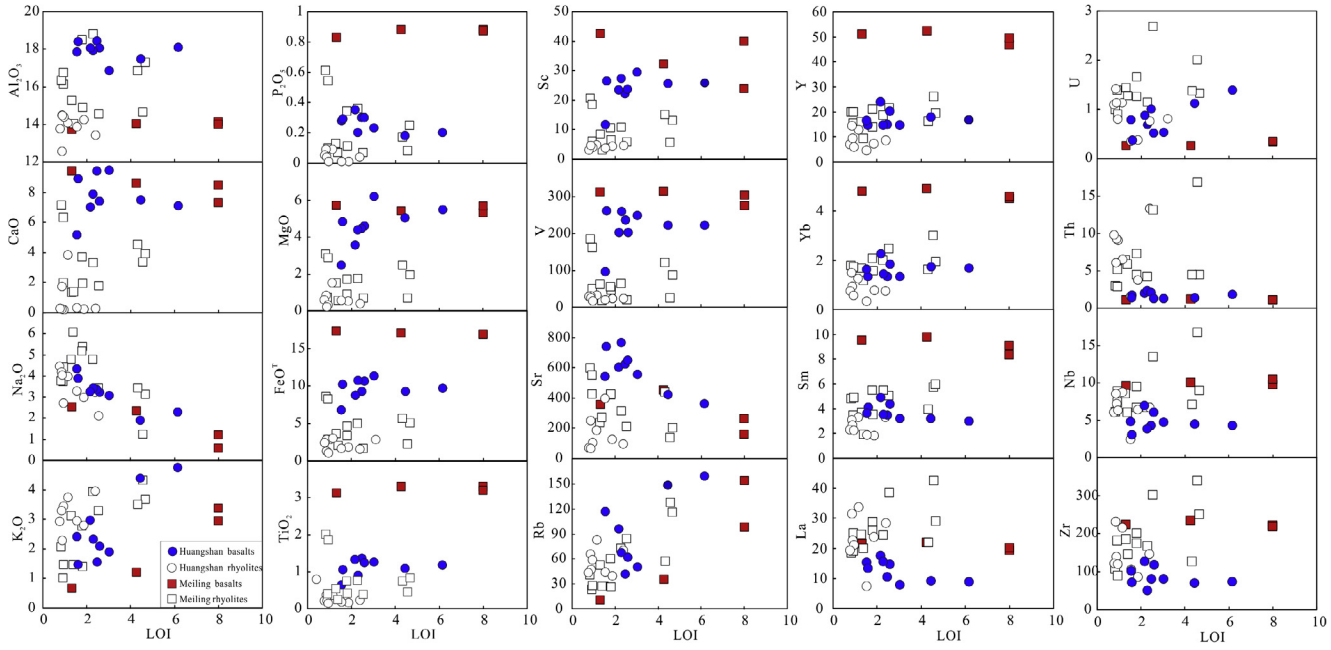

Fig. 6. Selected major and trace elements versus LOI variations showing the effects of alteration on whole-rock major and trace element compositions.

5.2. Origin of the basaltic rocks

5.2.1. Effects of fractionation and crustal contamination

Before determining source characteristics, it is important to assess the possible effects of fractional crystallization and crustal contamination on whole–rock geochemical compositions. The Huangshan and Meiling basalts have low MgO (mostly <6.0%) and Mg-number (39.7–54.3). Their Cr (9.95–108 ppm) and Ni (2.55–50.5 ppm) contents are significantly lower than those of primary mantle melts (e.g., Cr = 300–500 ppm, Ni = 300–400 ppm; Frey et al., 1978). These data suggest that parental magmas experienced significant fractional crystallization or crustal contamination.

The effects of fractional crystallization on whole-rock compositions of the Meiling basalts are poorly constrained because of the small range in major elements. Correspondingly, we discuss only the effects of fractional crystallization process on the whole-rock

compositions of the Huangshan basalts, because they have a large range in major element compositions.

The positive correlation between TiO_2, FeO^T and MgO (Fig. 7a, b) for Huangshan basalts establishes the fractional crystallization of magnetite (±clinopyroxenite), which indicates relatively high fO_2 of the primary magma. These basalts have positive correlation of CaO/Al_2O_3 and Sc versus MgO (Fig. 7c, d), indicating the presence of olivine and clinopyroxene in the assemblage of fractional

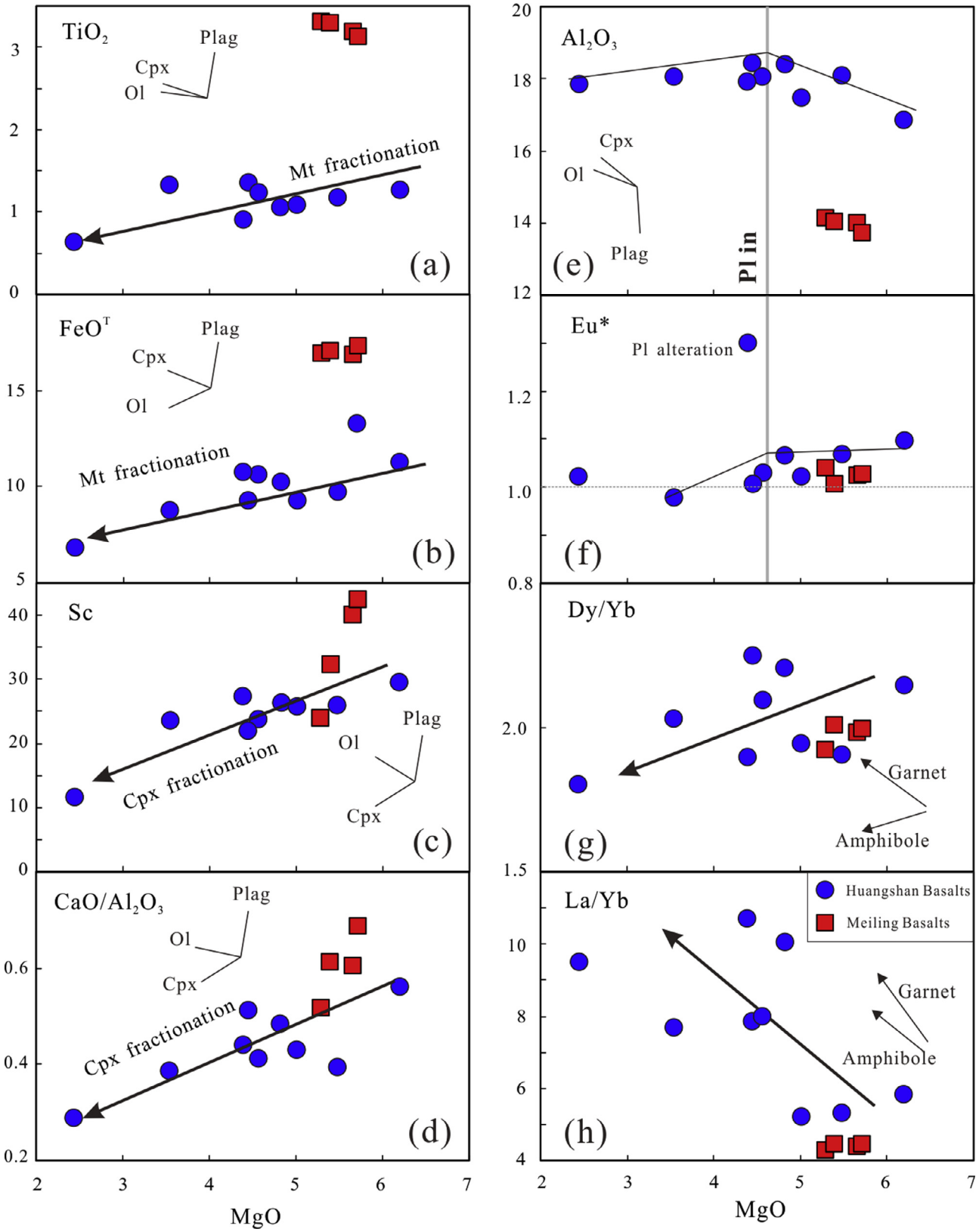

Fig. 7. Bivariation plots of TiO_2 (a), FeO^T (b), Sc (c), CaO/Al_2O_3 (d), Al_2O_3 (e), Eu^* (f), Dy/Yb (g) and La/Yb (h) versus MgO for the Huangshan and Meiling basalts.

crystallized minerals. They are also characterized by the presence of a reflection point on the MgO–Al_2O_3 plot (Fig. 7e). The Al_2O_3 contents of increase with decreasing MgO at MgO > 4.5, and then decrease with decreasing MgO at MgO < 4.5. This implies that plagioclase is saturated at MgO = 4.5, and that Al_2O_3 content of the system, therefore, reached the maximum value of 19%. This is confirmed by a weakly reflection point on the plot of Eu*–MgO (Fig. 7f), due to amphibole fractional offsetting the plagioclase influence. The Huangshan basalts have fractionated LREE/HREE ratios, with positive correlation of MgO vs. Dy/Yb (Fig. 7g), and negative correlation of MgO vs. La/Yb (Fig. 7h), indicating fractional crystallization of amphibole, without garnet during magma differentiation (Bachmann et al., 2005; Kratzmann et al., 2010; Smith, 2014).

The effect of continental crust contamination on the mantle-derived melts during ascent through continental crust can be examined by the correlation between elements or their ratios versus isotopes (Wang et al., 2008a, 2014). Here, we examine correlations between selected trace element ratios such as Nb/La, Nb/Th, Th/Ta, and Zr/Nb and Nd isotopes. These correlations could be caused by crustal or subcontinental lithospheric mantle (SCLM) contamination. Crustal contamination can result in correlations between major elements and isotopes, whereas contamination of asthenospheric mantle-derived melts by SCLM does not much change major element compositions (Wang et al., 2008a, 2015, 2016). Both Huangshan and Meiling basalts show different correlations of Nb/La versus Nb/Th, Th/Ta, Zr/Nb and $\varepsilon_{Nd}(t)$ (figures not shown), indicating crustal contamination or the involvement of SCLM components. The lack of obvious correlation in the bivariation diagrams of Nb/Th and Zr/Nb versus MgO (Fig. 8b, c) rules out the possibility of significant crustal contamination. More importantly, the nearly constant $\varepsilon_{Nd}(t)$ values with decreasing MgO contents (Fig. 8a) also argue against significant crustal and SCLM contamination.

In summary, the Huanshan basalts underwent a fractional crystallization sequence of olivine → olivine + clinopyroxene + magnetite at MgO > 4.5%, with the involvement of amphibole, followed by plagioclase-dominant crystal fractionation MgO < 4.5%. The effects of crustal contamination on parental magmas of the Huangshan and Meiling basalts are insignificant.

5.2.2. Hydrous vs. dry primary magma?

The 860 Ma Huangshan and 840 Ma Meiling basalts have similar isotopic characteristics, but have distinctive chemical compositions (Table 3, Fig. 8). As shown in Fig. 7 and Table 2, the Huangshan basalts are characterized by high SiO_2 and Al_2O_3 and low TiO_2 and FeO^T contents, a typical characteristic of derivation from hydrous magma (Wang et al., 2016). This is consistent with the sequence of mineral fractional crystallization, which involved early magnetite, clinopyroxene and amphibole, and then plagioclase at the late stage (MgO < 4.5%). By contrast, the Meiling basalts have lower SiO_2 and Al_2O_3 and higher TiO_2 and FeO^T contents relatively to the Huangshan basalts. This can be attributed to distinctive water contents of parental magmas, a controlling factor in the sequence of mineral fractional crystallization (Gaetani et al., 1993). Experimental results have shown that water-saturated magma systems can suppress plagioclase precipitation, and cause the early crystallization phase to be olivine, clinopyroxene, magnetite and spinel (e.g. Parman et al., 2011; Alonso-Perez et al., 2009). In contrast, in a dry magmatic system, plagioclase crystallizes earlier than clinopyroxene. The delay of plagioclase crystallization could result in enrichment of Al_2O_3 content as shown in the Huangshan basalts (Fig. 7e). In addition, water-saturated magmas are generally characterized by high fO_2. Such magmas should crystallize magnetite and probable amphibole at suitable pressure conditions in the early stage of the magmatic evolution (Alonso-Perez et al., 2009). Therefore, the evolved magma should be low in FeO^T and TiO_2. Furthermore, the evolution of the Huangshan basalts exclusively falls within the experiment-defined crystal fractionation trend of hydrous basaltic melts, whereas the evolution of the Meiling basalts is consistent with the trend defined by anhydrous experiments (Fig. 9a–c). The pre-eruption water contents in magma can be further constrained by using the maximal Al_2O_3 value along the liquid lines of descent (LLDs) (Parman et al., 2011; Wang et al., 2016 and references therein). The high Al_2O_3 contents can also be attributed to plagioclase accumulation, but this possibility can be ruled out by the presence of the negative correlation between Al_2O_3 and Eu* in the Huangshan basalts (see Figure in appendix) because the plagioclase accumulation results in positive correlation between Al_2O_3 and Eu*. As shown in Fig. 7e, the maximal Al_2O_3 on the LLDs of the Huangshan basalts is ~19%, corresponding to a pre-eruption magma water content of 3.6% (Parman et al., 2011). This implies that the Huangshan basalts were

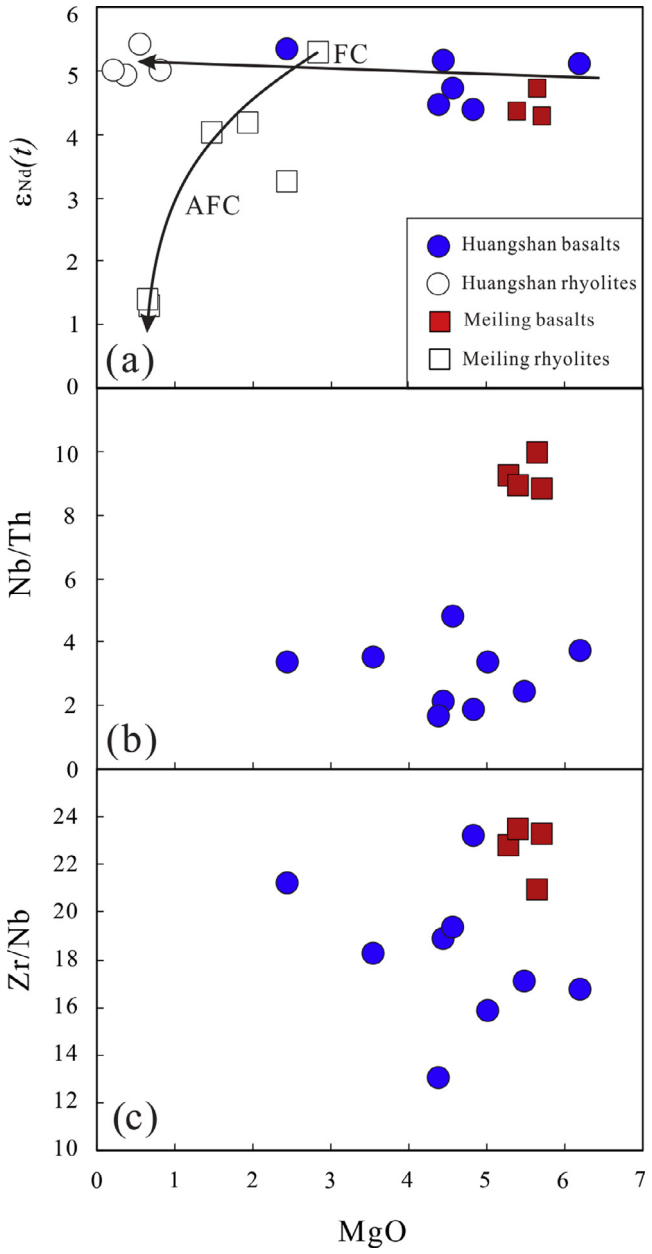

Fig. 8. Bivariation plots of $\varepsilon_{Nd}(t)$ (a), Nb/Th (b), Zr/Nb (c) versus MgO for the Huangshan and Meiling bimodal volcanic rocks.

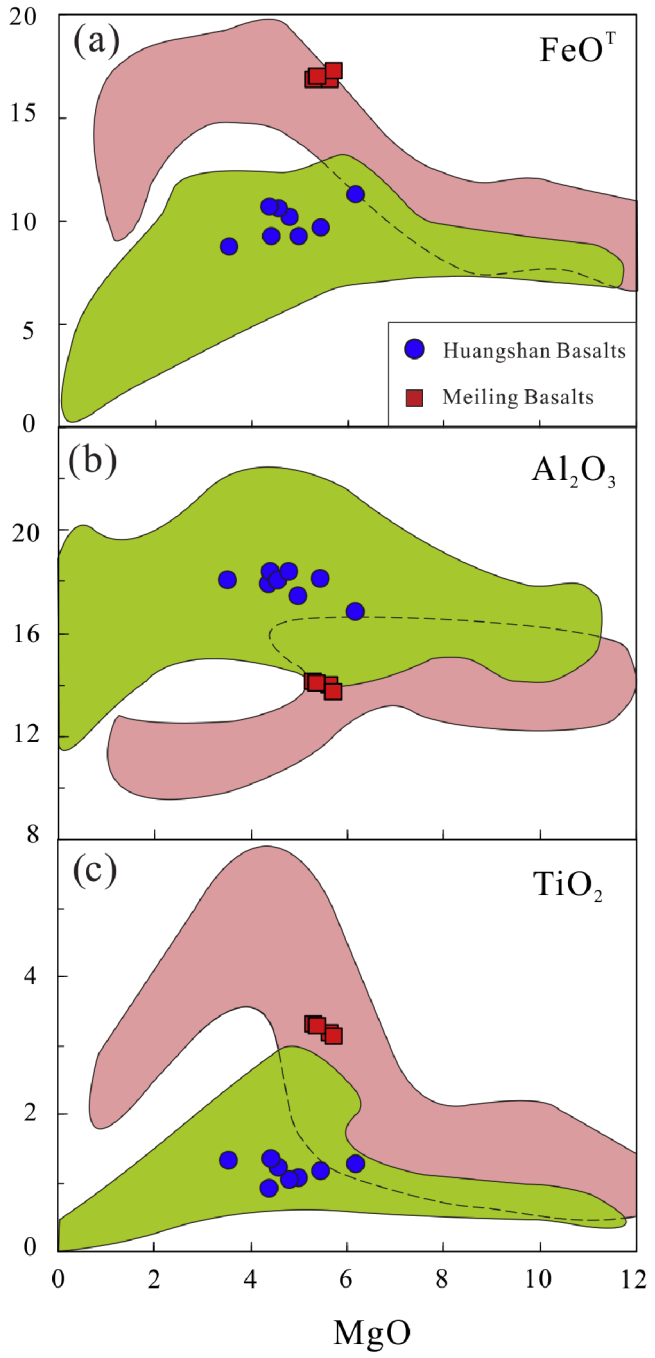

Fig. 9. Comparing FeO^T (a), Al_2O_3 (b) and TiO_2 (c) versus MgO for the Huangshan and Meiling basalts. The green area shows the range of experimentally determined LLDs of hydrous basalts. The red area shows the range of experimentally determined LLDs of anhydrous basalts. Fields of LLDs are after Wang et al. (2016).

derived from a hydrous depleted mantle, whereas the Meiling basalts originated from a normal (dry) depleted mantle.

5.3. Origin of the felsic rocks

The petrogenesis of felsic rocks in a bimodal volcanic suite is quite controversial (Bonnefoi et al., 1995). Two models have been proposed to explain the origin of the felsic end-member: (1) fractional crystallization of basaltic magmas with minor or without crustal contamination (Peccerillo et al., 2003, and the references therein), and (2) partial melting of pre-existing crustal rocks (Suneson and Lucchitta, 1983; Li et al., 2002a).

5.3.1. Origin of the Huangshan felsic rocks

As shown in Fig. 10a, Huangshan felsic and mafic rocks have similar $\varepsilon_{Nd}(t)$ values regardless of their distinctive trace and major element compositions, implying that the felsic rocks were likely formed by fractional crystallization of their basaltic counterparts. However, major and trace elements of the Huangshan felsic rocks are characterized by high A/CNK values (>1.1) and a wide SiO_2 gap between the mafic- and felsic-member (~15% interval). Such characteristics cannot be sufficiently explained by fractional crystallization processes, because felsic rocks formed by the evolution of basaltic parental magma through fractional crystallization processes usually have an I-type granite feature with an A/CNK value < 1.1 (Chappell, 1999; Li et al., 2007), because feldspar (A/CNK = 1) precipitation could prevent the enrichment of alumina in melts (Zen, 1986). Furthermore, felsic rocks formed by fractional crystallization of basaltic magmas are commonly assumed to generate a continuum in chemical composition, and the REE patterns of the felsic rocks should resemble their basaltic parental magma (Bonnefoi et al., 1995; Chayes, 1963).

As mentioned above, the similarity of Nd isotopic compositions between co-existing felsic and mafic rocks rules out the possibility of partial melting of ancient supracrustal materials. There still exists the possibility that the felsic rocks were formed by partial melting of juvenile crust (i.e., underplated igneous rocks). However, the Huangshan felsic end-member has high and variable A/CNK values (up to 1.71), a typical characteristic of S-type granites formed by partial melting of crustal sedimentary rocks rather than juvenile igneous rock. Experimental and case studies indicate that peraluminous magma can also be produced by fractional crystallization of a meta-aluminous, water-saturated parental magma, because water can restrain plagioclase (A/CNK = 1) crystallization, and enhance amphibole (A/CNK = 0.5, Zen, 1986) crystallization, leading the melts to evolve towards a higher A/CNK value (Zen, 1986). Furthermore, the fractional crystallization of an amphibole-dominated mineral assemblage (including magnetite) can also quickly increase SiO_2 contents of residual melts to produce a SiO_2 composition gap, because amphibole has low SiO_2 contents (Dufek and Bachmann, 2010). This scenario is also supported by experimental and numerical simulations that show that the evolution of primary magmas with moderate water contents (~2.3%) features a large SiO_2 compositional gap (Melekhova et al., 2013). Therefore, the presence of high and variable A/CNK values and a large SiO_2 compositional gap in the Huangshan volcanic rocks can be explained by fractionation of a water-saturated parental magma through amphibole-dominated fractional crystallization. This is also consistent with the parental magma composition and fractioned mineral assemblage of the Huangshan basaltic rocks as discussed above.

The fractioned crystallization of an amphibole-dominated mineral assemblage can also change the REE pattern of the resultant magmas (Glazner et al., 2008; Bachmann et al., 2005). The slightly scoop-shaped REE patterns of the Huangshan felsic rocks (Fig. 5e) are similar to those observed in the Fish Canyon Tuff (FCT) glass and the Half Dome Granodiorites (avg HD) that were formed by fractionation of amphibole with possible minor titanite (Glazner et al., 2008; Bachmann et al., 2005). Therefore the presence of the scoop-shaped REE patterns, correlations between La/Yb, Dy/Yb versus MgO (Fig. 7g, h), and positive Zr–Hf anomalies (Fig. 5f) imply that the formation of the Huangshan felsic rocks involved fractionation of amphibole and titanite without garnet (Bachmann et al., 2005).

In summary, the Nd isotope and element geochemical features of the Huangshan felsic rocks indicate that they were likely formed

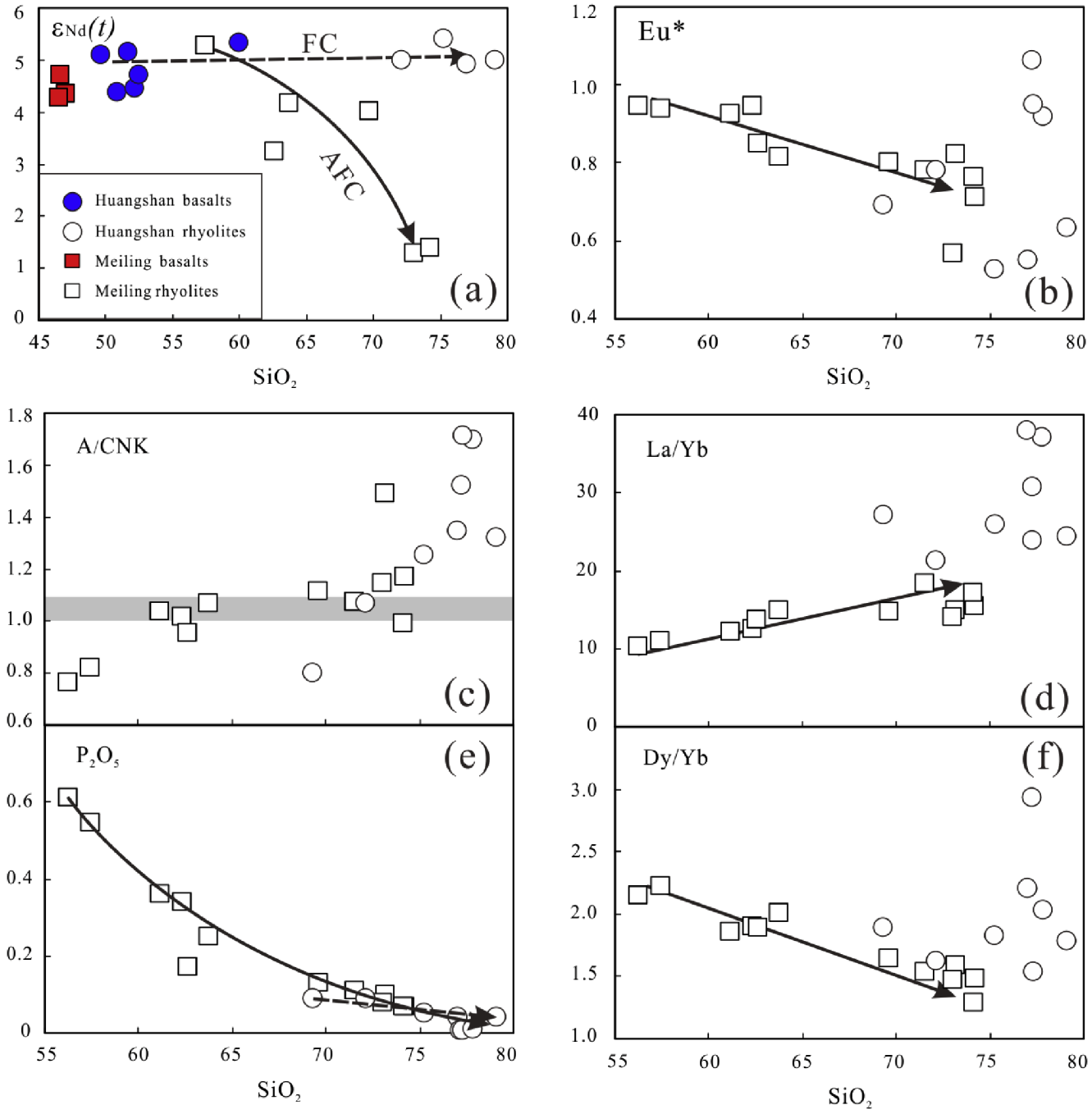

Fig. 10. Bivariation plots of $\varepsilon_{Nd}(t)$ (a), Eu^* (b), A/CNK (c), La/Yb (d), P_2O_5 (e), Dy/Yb (f) versus SiO_2 for Huangshan and Meiling bimodal volcanic rocks.

by fractional crystallization of a water-saturated Huangshan basaltic magma, involving an amphibole-dominated mineral assemblage.

5.3.2. Origin of the Meiling felsic rocks

The least-evolved Meiling felsic rocks are meta-aluminous and show negative correlation in P_2O_5 vs. SiO_2 diagram, suggesting that they are likely I-type granitic rocks, which are formed by fractional crystallization of mafic parental magmas or partial melting of crustal igneous rocks. The Meiling rocks show slight Eu depletion (Eu^* = 0.94–0.56) (Table 2; Fig. 5g) and negative correlation of SiO_2 with Eu^* (Fig. 10b), suggesting plagioclase crystallization. Moreover, the scoop-shaped REE patterns of these rocks also suggest the involvement of amphibole and minor titanite crystallization, thereby resembling those of the Huangshan felsic rocks. The fractional crystallization of amphibole can be further confirmed by the presence of positive correlations of La/Yb vs. SiO_2 and negative correlation of Dy/Yb vs. SiO_2 in the Meiling felsic rocks (Fig 10d, f,). Amphibole as a mainly fractionated mineral in magma implies that the magma was hydrous; therefore it cannot have formed by fractional crystallization of coeval anhydrous Meiling mafic magma, rather partial melting of hydrous mafic igneous rocks is required. Considering the depleted $\varepsilon_{Nd}(t)$ values of the least evolved samples of the Meiling felsic rocks, a possible candidate for the Meiling felsic rocks is the ~860 Ma underplated hydrous basaltic rocks.

The Meiling basaltic to andestic rocks have similar $\varepsilon_{Nd}(t)$ with increasing silica contents, whereas the felsic rocks have negative

correlation of $\varepsilon_{Nd}(t)$–SiO_2 (Fig. 10a), thereby differing from Huangshan volcanic rocks. The negative correlation between Nd isotopic compositions and silica contents suggests that ancient crustal material contamination probably played a key role in the petrogenesis of the felsic rocks.

Therefore, the Meiling felsic rocks were probably formed by partial melting of ~860 Ma underplated hydrous basaltic rocks, then underwent dominant amphibole and plagioclase fractional crystallization, and were contaminated with ancient crustal materials.

6. Geological implications

6.1. Multiple phases of intraplate extension-related magmatism prior to mantle plume magmatism

Meiling basalts have typical OIB-like geochemical features which plot them in the OIB and intraplate fields of tectonic discrimination diagrams (Fig. 11). In contrast, the Huangshan basalts are characterized by arc-like trace element signatures, as discussed above. Such arc-like trace element features are usually observed in back-arc basin basalts (BABB) and true arc basalts (Kelley et al., 2006; Parman et al., 2011; Saunders and Tarney, 1984; Taylor and Martinez, 2003), but recent research indicates that these features are also present in many large intraplate igneous provinces, such as Karoo, Siberia, CAMP (Central Atlantic magmatic province), Columbia River, Emeishan, Deccan, and Basin and Range (Wang et al., 2016). The Ti/V ratio is sensitive to oxygen fugacity (fO_2) and therefore can be used to distinguish intraplate and arc basalts (Shervais, 1982). The Huangshan basalts have Ti/V ratios of 21–38, similar to those of MORB and CFBs (Ti/V = 20–50), but higher than those of volcanic rocks from modern island arcs (Ti/V ≤ 20). Further examinations based on the Zr vs. Zr/Y and Ti vs. V discrimination diagrams (Fig. 11b, c) can successfully distinguish arc-like continental basalts from true arc basalts, because the primary melts of arc-like continental basalts have higher Zr and Ti contents than those of true arc basalts (Wang et al., 2016). The Huangshan and Meiling basalts plot into the intraplate field or offset from the volcanic arc basalt field on the Zr vs. Zr/Y and Ti vs. V discrimination diagrams (Fig. 11b, c), suggesting that the basalts were most likely formed within an intraplate setting. This conclusion is consistent with general geological observations: (1) a contemporaneous rift basin initiated at ~860 Ma (Luojiamen conglomerates, our unpublished data); (2) collision-related magmatism ceased at ~890 Ma, as established from ~890 Ma obduction-type granites in the NE Jiangxi ophiolite (Li et al., 2008a), and the youngest Neoproterozoic Shuangxiwu arc magmatism (Li et al., 2009a); (3) ~850 Ma rift-related magmatism in the southeast Yangtze Block (Li et al., 2009a, 2010b,c).

Despite existing different viewpoints on the origin of the Neoproterozoic magmatism (Chen and Jahn, 1998; Li et al., 2002b, 2008a, 2009a,; Zhao and Zhou, 2007a,b; Zhou et al., 2002a,b, 2006), ~825 Ma volcano-plutonic magmatism (Fig. 12b), 825 Ma komatiitic basalts (Yiyang komatiitic basalts, Wang et al., 2007) and 821–811 Ma continental flood basalts (CFBs) (Bikou CFBs, Wang et al., 2008a) in South China (Fig. 1) imply that high-temperature mantle upwelling (i.e., mantle plume) at ~825 Ma (Li et al., 1999, 2003b,c, 2005a, 2008a, 2010b; Wang et al., 2007, 2008a, 2009). Prior to the 825 Ma magmatic event, small volume ~850 Ma magmatic events associated with rift-related sedimentation are also documented (Li et al., 2009a, 2010b,c; Wang et al., 2013 Zhang et al., 2013). The ~860 Ma and ~840 Ma bimodal volcanic rocks in southeastern Yangtze Block documented here, along with compiled magmatic ages from the southern margin of the Yangtze Block (Fig. 12a, b) show that multi-phase anorogenic

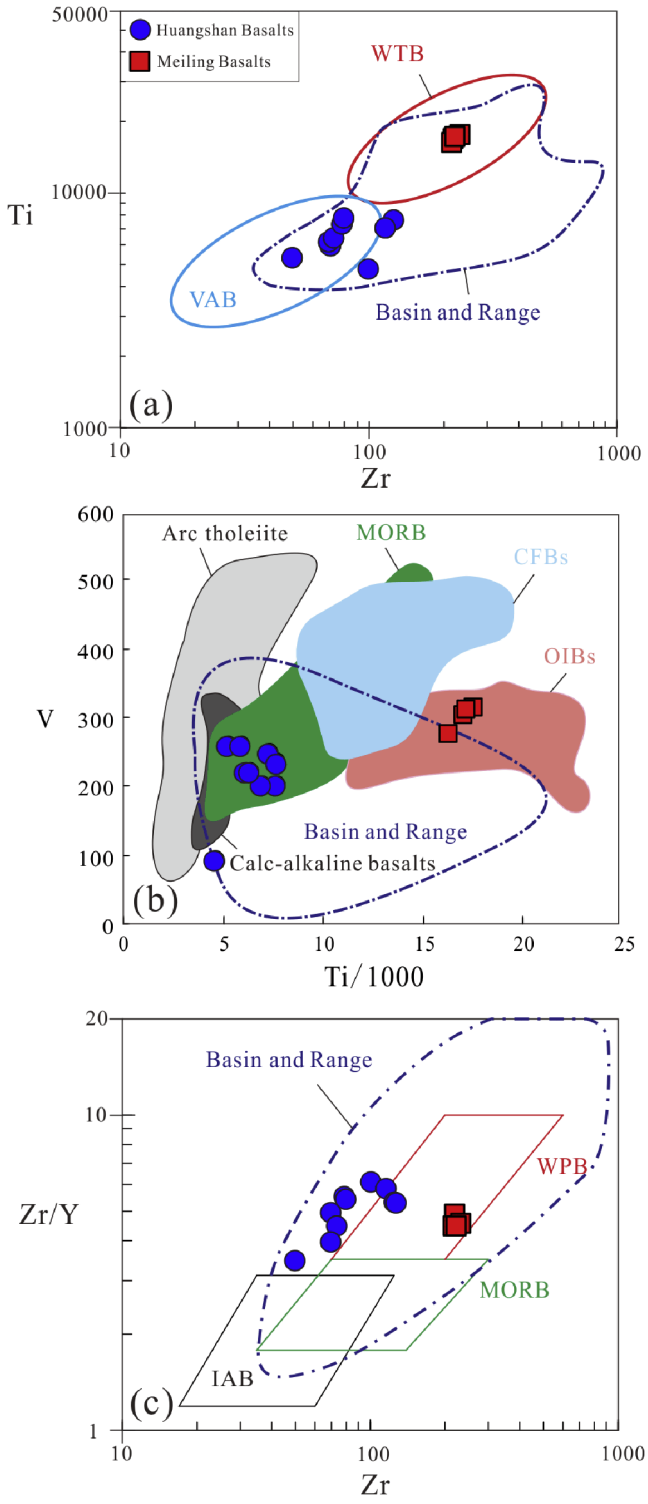

Fig. 11. Plots of (a) Zr – Ti (Pearce, 1996), (b) Ti/1000 – V (Shervais, 1982), (c) Zr – Zr/Y (Pearce and Norry, 1979). Fields of arc tholeiitic basalts, calc-alkaline basalts, MORB, continental flood basalts (CFBs), Oceanic Island basalts (OIBs), Within Plate basalts (WPB), Island Arc basalts (IAB), and Basin and Range basalts are after Wang et al. (2016).

magmatic events occurred between the finial assemblage of the Yangtze and Cathaysia blocks (~890 Ma) and the arrival of the mantle plume (~825 Ma). In common with South China, ~900–840 Ma extension-related magmatism is also reported in other blocks of Rodinia (Li et al., 2010b), including: (1) abundant

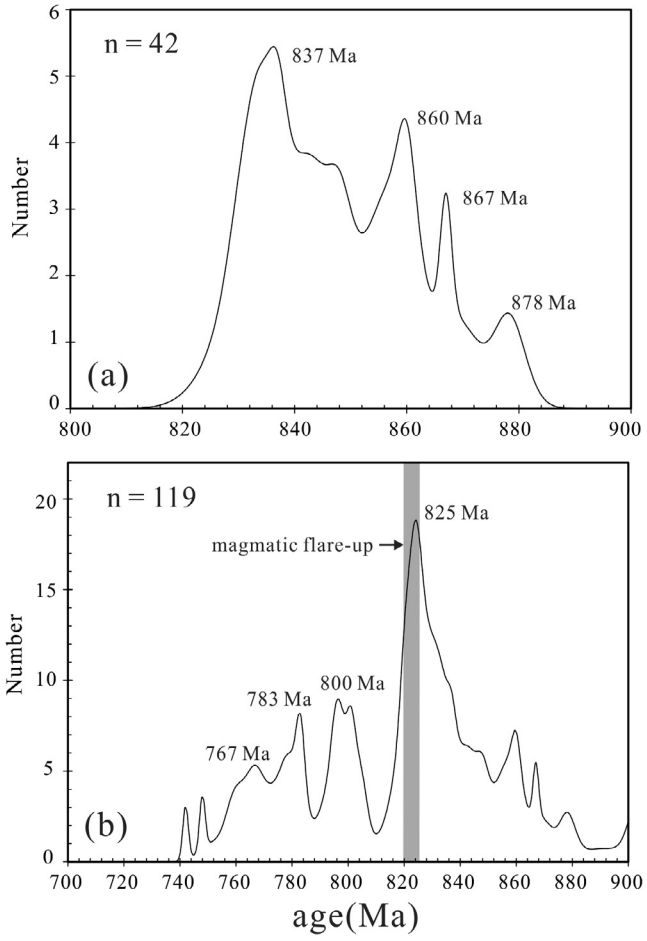

Fig. 12. Probabilistic histogram of age distributions for the 830–900 Ma (a) and 740–900 Ma (b) igneous rocks in the southern margin of the Yangtze Block, South China. Data source: appendix table 1.

~870 Ma MORB-like basaltic dikes and anatectic granites in the Scottish promontory of Laurentia (Friend et al., 1997; Millar, 1999; Soper et al., 1998; Dalziel and Soper, 2001; Cawood et al., 2015); (2) ~870 Ma rift-related felsic volcanic rocks in the Zambezi Belt along the southern margin of the Congo Craton (Johnson and others, 2005, 2007; De Waele et al., 2008); (3) ~850 Ma granites in the Seve–Kalak Superterrane of the Baltica Block, which are interpreted as being formed in a extensional setting (Paulsson and Andreasson, 2002); (4) ~870 Ma intermediate to felsic volcanic rocks in the Chukotka terrane of the Arctic Alaska, which are also considered to be related to the breakup of Rodinia (Amato et al., 2009). These early magmatic rocks provide crucial information for understanding the driving force for the formation of the mantle plume, which triggered the massive anorogenic magmatism and final breakup of the Rodinia supercontinent.

6.2. Water played a key role in the origin of pre-mantle-plume anorogenic magmatism in Neoproterozoic South China

It is generally accepted that mantle plumes play an important role in the breakup and dispersal of supercontinents (Storey, 1995; Korenaga, 2004). The petrological expressions of mantle plume events are massive basaltic rocks (e.g., CFBs) associated with high-temperature igneous rocks, such as komatiites (generally in Precambrian sequences) and picrites (generally in Phanerozoic sequences). However, the mechanism that drives the upwelling of deep mantle magma is still widely debated. Previous studies found that many CFBs comprise two types of basalt, namely OIB-like and arc-like basalts (Puffer, 2001). Because of the separation from active continental margins, arc-like signatures of CFBs were attributed to contamination by crustal rocks or by subcontinental lithospheric mantle metasomatized by early subducted slab-derived fluids/melts (Hawkesworth et al., 1992; Jourdan et al., 2007; Lightfoot et al., 1990; Murphy and Dostal, 2007; Turner and Hawkesworth, 1995; Turner et al., 1996; Wang et al., 2008a, 2009, 2014). Recent studies of Sr–Nd–Pb–Os isotopes from the ~180 Ma Karoo CFBs (Heinonen et al., 2014) and ~200 Ma Central Atlantic Magmatic Province (CAMP) CFBs (Merle et al., 2014) indicate that crustal rocks or the subcontinental lithospheric mantle played a minor role in the formation of these arc-like basalts. This is confirmed by an oxygen isotope study of Karoo and Etendeka picrites (Harris et al., 2015) and model calculations of the Karoo enriched CFBs (Heinonen et al., 2016). Rather, it is mainly attributed to chemical heterogeneity as a result of mixing between depleted mantle reservoirs beneath lithosphere and recycled subduction-modified oceanic crust (Heinonen et al., 2014, 2016; Merle et al., 2014; Harris et al., 2015; Wang et al., 2016).

Here, we show that heterogeneity existed not only in the chemical composition but also in fluid contents of the source regions of the ~860 Ma Huangshan basalts and the ~840 Ma Meiling basalts. Therefore, water, or volatile fluid, could have played a key role in the formation of arc-like basalts in Neoproterozoic South China. Considering that the Huangshan and Meiling basalts formed earlier than the ~825 Ma magmatism that is interpreted to have been the consequence of a mantle plume, we postulate that water, or volatile fluid, may have fluxed into the asthenospheric mantle and triggered the partial melting. However, the origin of the water is poorly constrained due to the mobility of most incompatible elements (e.g., Sr, Rb and Ba) caused by the strong deformation and upper greenschist-facies metamorphism recorded by the studied rocks. Wang et al. (2016) proposed that avalanche of a "stagnant slab" at a mantle transition zone (MTZ, 440–660 km) could release fluids and drive a wet upwelling, which would then pond at the l ithosphere–asthenosphere boundary (LAB). We therefore consider that MTZ-derived fluid probably pooled at the LAB beneath the South China Block at ~ 860 Ma, which triggered lithospheric extension to form early stage rifting and associated bimodal volcanic rocks.

7. Conclusions

(1) SIMS U–Pb zircon geochronology indicates that the Huangshan and the Meiling bimodal volcanic rocks in southeastern Yangtze Block, South China were formed respectively at 860 ± 9 Ma and 840 ± 5 Ma.

(2) The ~860 Ma Huangshan bimodal volcanic rocks are a calc-alkaline series characterized by a large range of SiO_2 contents with a gap between 55% and 70%. The basaltic rocks derived from a hydrous depleted mantle source and then underwent fractional crystallization during magma ascent. The estimated pre-eruption magma H_2O concentrations using LLD method was ~3.60%. The Huangshan felsic rocks have identical $\varepsilon_{Nd}(t)$ values to their basaltic counterparts, and probably formed by fractional crystallization of the Huangshan basaltic rocks.

(3) The ~840 Ma Meiling bimodal volcanic rocks have a narrow SiO_2 compositional gap between 50% and 55%. The basaltic end-member is characterized by tholeiitic and OIB-like geochemical signatures with depleted Nd isotopic composition; they were most likely produced by partial melting of a normal (dry) depleted mantle source. The elemental and Nd isotopic characteristics of the felsic end-member suggest that

the felsic rocks were most likely formed by partial melting of a juvenile hydrous mafic igneous source, possibly the ~860 Ma underplating intrusive basaltic rocks, and then contaminated, to some extent, by ancient crustal rocks.

(4) Our study establishes multi-phase rift-related anorogenic magmatism occurred before the ~825 Ma mantle-plume related magmatism in South China. Water released from subducted slabs in deep Earth, (probably from the mantle transition zone), played a key role on hydrating the shallow part of the asthenospheric mantle, and triggered the mantle melting to generate magmas, and probably drove the mantle plume formation and the final breakup of the Rodinia supercontinent.

Acknowledgements

We would like to thank Prof. B. Krapež for careful proofreading, two anonymous reviewers for careful and instructive reviews, J.H Tao for assistance in field work, X.Y Wang, X. L. Tu, Z.Y Ren and L Zhang for their assistance in major and trace element geochemical and Sr–Nd isotopic analyses, and Q.L Li and X.P Xia in SIMS U–Pb zircon analyses. This work was supported by the National Key Research and Development Program of China (2016YFC0600204), the Chinese Academy of Sciences (QYZDY-SSW-DQC017), National Natural Science Foundation of China (grants 41573026 and 41373033), and ARC Future Fellowship (FT140100826) and the Fundamental Research Funds for the Central Universities (program for Innovative Research Team of chemical geodynamics and Earth resources: 310827163412) to X.C.Wang. This is GIGCAS contribution NO. IS–2389.

Appendix A. Supplementary data

Supplementary data associated with this article can be found, in the online version, at http://dx.doi.org/10.1016/j.precamres.2017.04.039.

References

Alonso-Perez, R., Müntener, O., Ulmer, P., 2009. Igneous garnet and amphibole fractionation in the roots of island arcs: experimental constraints on andesitic liquids. Contrib. Mineral. Petr. 157 (4), 541–558.

Amato, J.M., Toro, J., Miller, E.L., Gehrels, G.E., Farmer, G.L., Gottlieb, E.S., Till, A.B., 2009. Late Proterozoic-Paleozoic evolution of the Arctic Alaska-Chukotka terrane based on U-Pb igneous and detritial zircon ages: implications for Neoproterozoic paleogeographic reconstructions. Geol. Soc. Am. Bull. 121, 1219–1235.

Bachmann, O., Dungan, M.A., Bussy, F., 2005. Insights into shallow magmatic processes in large silicic magma bodies: the trace element record in the Fish Canyon magma body. Colorado. Contrib. Mineral. Petr. 149 (3), 338–349.

Black, L.P., Kamo, S.L., Allen, C.M., Davis, D.W., Aleinikoff, J.N., Valley, J.W., Mundil, R., Campbel, I.H., Korsch, R.J., Williams, I.S., Chris, Foudoulis, 2004. Improved $^{206}Pb/^{238}U$ microprobe geochronology by the monitoring of a trace-element-related matrix effect; SHRIMP, ID-TIMS, ELA-ICP-MS and oxygen isotope documentation for a series of zircon standards. Chem. Geol. 205 (1–2), 115–140.

Bonnefoi, C.C., Provost, A., Albarède, F., 1995. The 'Daly gap' as a magmatic catastrophe. Nature 378 (6554), 270–272.

Cawood, P.A., Strachan, R.A., Merle, R.E., Millar, I.L., Loewy, S.L., Dalziel, I.W.D., Kinny, P.D., Jourdan, F., Nemchin, A.A., Connelly, J.N., 2015. Neoproterozoic to early Paleozoic extensional and compressional history of East Laurentian margin sequences: the Moine Supergroup, Scottish Caledonides. Geol. Soc. Am. Bull. 127 (3–4), 349–371.

Chappell, B.W., 1999. Aluminium saturation in I– and S–type granites and the characterization of fractionated haplogranites. Lithos 46 (3), 535–551.

Chayes, F., 1963. On pyroxene molecules in the CIPW Norm. Geol. Mag. 100 (1), 7–10.

Chen, J.F., Jahn, B.M., 1998. Crustal evolution of southeastern China: Nd and Sr isotopic evidence. Tectonophysics 284 (1), 101–133.

Cheng, H., 1991. The late Proterozoic collision orogen in northwestern Zhejiang Province. Geol. Rev 37 (3), 203–213.

Condie, K.C., 1998. Episodic continental growth and supercontinents: a mantle avalanche connection? Earth Planet. Sc. Lett. 163 (1), 97–108.

Condie, K.C., 2003. Supercontinents, superplumes and continental growth: the Neoproterozoic record. Geol. Soc. Lond. Spec. Publ. 206 (1), 1–21.

Condie, K.C., 2004. Supercontinents and superplume events: distinguishing signals in the geologic record. Phys. Earth Planet. Interiors 146 (1), 319–332.

Crawford, A.J., Hilyard, D., 1990. Geochemistry of late Proterozoic tholeiitic flood basalts, Adelaide Geosyncline SouthAustralia. In: Jago, J.B., Moore, P.S. (Eds.), The Evolution of a Late Precambrian-Early Palaeozoic Rift Complex: The Adelaide Geosyncline, vol. 16. Geol. Soc. Aust. Spec. Publ., pp. 49–67.

Dalziel, I.W.D., Soper, N.J., 2001. Neoproterozoic extension on the Scottish Promontory of Laurentia: paleogeographic and tectonic implications. J. Geol. 109, 299–317.

De Waele, B.D., Johnson, S.P., Pisarevsky, S.A., 2008. Palaeoproterozoic to Neoproterozoic growth and evolution of the eastern Congo Cration: its role in the Rodinia puzzle. Precambrian Res. 160, 127–141.

Dufek, J., Bachmann, O., 2010. Quantum magmatism: magmatic compositional gaps generated by melt–crystal dynamics. Geology 38 (8), 687–690.

Evans, D.A.D., 2009. The palaeomagnetically viable, long–lived and all–inclusive Rodinia supercontinent reconstruction. Geol. Soc. Lond. Spec. Publ. 327 (1), 371–404.

Evans, D.A.D., 2013. Reconstructing pre–Pangean supercontinents. Geol. Soc. Am. Bull. 125 (125), 1735–1751.

Eyles, N., Januszczak, N., 2004. 'Zipper–rift': a tectonic model for Neoproterozoic glaciations during the breakup of Rodinia after 750 Ma. Earth Sci. Rev. 65 (1–2), 1–73.

Frey, F.A., Green, D.H., Roy, S.D., 1978. Integrated models of basalt petrogenesis: a study of quartz tholeiites to olivine melilitites from South Eastern Australia utilizing geochemical and experimental petrological data. J. Petrol. 19 (3), 463–513.

Friend, C.R.L., Kinny, P.D., Rogers, G., Strachan, R.A., Paterson, B.A., 1997. U-Pb zircon geochronological evidence for Neoproterozoic events in the Glenfinnan Group (Moine Supergroup): the formation of the Ardgour granite gneiss, north–west Scotland. Contrib. Mineral Petr. 128, 101–113.

Gaetani, G.A., Grove, T.L., Bryan, W.B., 1993. The influence of water on the petrogenesis of subduction–related igneous rocks. Nature 365 (6444), 332–334.

Gao, L.Z., Yang, M.G., Ding, X.Z., Liu, Y.X., Xun, L., Ling, L.H., Chuan, H.Z., 2008. SHRIMP U-Pb zircon dating of tuff in the Shuangqiaoshan and Heshangzhen groups in South China – constraints on the evolution of the Jiangnan Neoproterozoic orogenic belt. Geol. Bull. China 27, 1744–1751 (in Chinese with English abstract).

Glazner, A.F., Coleman, D.S., Bartley, J.M., 2008. The tenuous connection between high–silica rhyolites and granodiorite plutons. Geology 36 (2), 183–186.

Harris, C., Roux, P.L., Cochrane, R., Martin, L., Duncan, A.R., Marsh, J.S., Roex, A.P.L., Class, C., 2015. The oxygen isotope composition of Karoo and Etendeka picrites: high δ 18 O mantle or crustal contamination? Contrib. Mineral. Petr. 170 (1), 1–24.

Hawkesworth, C.J., Gallagher, K., Kelley, S., Mantovani, M., Peate, D.W., Regelous, M., Rogers, N.W., 1992. Paraná magmatism and the opening of the South Atlantic. Geol. Soc. Lond. Spec. Publ. 68 (1), 221–240. Special Publications.

Hawkesworth, C.J., Dhuime, B., Pietranik, A.B., Cawood, P.A., Kemp, A., Storey, C.D., 2010. The generation and evolution of the continental crust. J. Geol. Soc. London 167 (2), 229–248.

Heinonen, J.S., Carlson, R.W., Riley, T.R., Luttinen, A.V., Horan, M.F., 2014. Subduction–modified oceanic crust mixed with a depleted mantle reservoir in the sources of the Karoo continental flood basalt province. Earth Planet. Sc. Lett. 394 (10), 229–241.

Heinonen, J.S., Luttinen, A.V., Bohrson, W.A., 2016. Enriched continental flood basalts from depleted mantle melts: modeling the lithospheric contamination of Karoo lavas from Antarctica. Contrib. Mineral. Petr. 171 (1), 1–22.

Hoffman, P.F., Kaufman, A.J., Halverson, G.P., Schrag, D.P., 1998. A Neoproterozoic snowball earth. Science 281 (5381), 1342–1346.

Jacobsen, S.B., Wasserburg, G.J., 1984. Sm–Nd isotopic evolution of chondrites and achondrites. Earth Planet. Sci. Lett. 67, 137–150.

Johnson, S.P., Rivers, T., De Waele, B., 2005. A review of the Mesoproterozoic to early Palaeozoic magmatic and tectonothermal history of south–central Africa: implications for Rodinia and Gondwana. J. Geol. Soci. Lond. 162, 433–450.

Johnson, S.P., De Waele, B., Evans, D., Banda, W., Tembo, F., Milton, J.A., Tani, K., 2007. Geochronology of the Zambezi Supercrustal sequence, southern Zambia: a record of Neoproterozoic divergent processes along the Southern Margin of the Congo Craton. J. Geol. 115, 355–374.

Jourdan, F., Bertrand, H., Schärer, U., Blichert-Toft, J., Féraud, G., Kampunzu, A.B., 2007. Major and trace element and Sr, Nd, Hf, and Pb isotope compositions of the Karoo Large Igneous Province, Botswana–Zimbabwe: lithosphere vs mantle plume contribution. J. Petrol. 48 (6), 1043–1077.

Karlstrom, K.E., Bowring, S.A., Dehler, C.M., Knoll, A.H., Porter, S.M., Des Marais, D.J., Weil, A.B., Sharp, Z.D., Geissman, J.W., Elrick, M.B., 2000. Chuar group of the Grand Canyon: record of breakup of Rodinia, associated change in the global carbon cycle, and ecosystem expansion by 740 Ma. Geology 28 (7), 619–622.

Kelemen, P.B., Hanghøj, K., Greene, A.R., 2003. One view of the geochemistry of subduction–related magmatic arcs, with an emphasis on primitive andesite and lower crust. Treatise Geochem. 138, 1–70.

Kelley, K.A., Terry, P., Grove, T.L., Stolper, E.M., Sally, N., Erik, H., 2006. Mantle melting as a function of water content beneath back-arc basins. J. Geophys. Res. Solid Earth 111 (B9), 535–540.

Korenaga, J., 2004. Mantle mixing and continental breakup magmatism. Earth Planet. Sc. Lett. 218 (3–4), 463–473.

Kratzmann, D.J., Carey, S., Scasso, R.A., Naranjo, J.A., 2010. Role of cryptic amphibole crystallization in magma differentiation at Hudson volcano, Southern Volcanic Zone. Chile. Contrib. Mineral. Petr. 159 (2), 237–264.
Lamotte, D.F.D., Fourdan, B., Leleu, S., Leparmentier, F., Clarens, P.D., 2015. Style of rifting and the stages of Pangea breakup. Tectonics 34 (5), 1009–1029.
Li, X.H., 1997. Geochemistry of the Longsheng Ophiolite from the southern margin of Yangtze Craton, SE China. Geochem. J. 31 (5), 323–337.
Li, Z.X., Zhang, L.H., Powell, C. Mca., 1995. South China in Rodinia: part of the missing link between Australia-East Antartica and Laurentia? Geology 23 (5), 407.
Li, Z.X., Li, X.H., Kinny, P.D., Wang, J., 1999. The breakup of Rodinia: did it start with a mantle plume beneath South China? Earth Planet. Sc. Lett. 173 (3), 171–181.
Li, X.H., Li, Z.X., Zhou, H., Liu, Y., Kinny, P.D., 2002a. U-Pb zircon geochronology, geochemistry and Nd isotopic study of Neoproterozoic bimodal volcanic rocks in the Kangdian Rift of South China: implications for the initial rifting of Rodinia. Precambrian Res. 113 (1–2), 135–154.
Li, Z.X., Li, X.H., Zhou, H., Kinny, P.D., 2002b. Grenvillian continental collision in South China: new SHRIMP U-Pb zircon results and implications for the configuration of Rodinia. Geology 30 (2002), 163–166.
Li, X.H., Li, Z.X., Zhou, H.W., Liu, Y., Liang, X.R., Li, W.X., 2003a. SHRIMP U-Pb zircon age, geochemistry and Nd isotope of the Guandaoshan pluton in SW Sichuan: Petrogenesis and tectonic significance. Sci. China (Earth Sci.) 46 (1), 73–83.
Li, X.H., Li, Z.X., Ge, W., Zhou, H., Li, W., Liu, Y., Wingate, M.T.D., 2003b. Neoproterozoic granitoids in South China: crustal melting above a mantle plume at ca. 825 Ma? Precambrian Res. 122 (1–4), 45–83.
Li, Z.X., Li, X.H., Kinny, P.D., Wang, J., Zhang, S., Zhou, H., 2003c. Geochronology of Neoproterozoic syn–rift magmatism in the Yangtze Craton, South China and correlations with other continents: evidence for a mantle superplume that broke up Rodinia. Precambrian Res. 122 (1–4), 85–109.
Li, X.H., Liu, D.B., Sun, M., Li, W.X., Liang, X.R., Liu, Y., 2004. Precise Sm–Nd and U-Pb isotopic dating of the supergiant Shizhuyuan polymetallic deposit and its host granite. SE China. Geol. Mag. 141 (2), 225–231.
Li, W.X., Li, X.H., Li, Z.X., 2005. Neoproterozoic bimodal magmatism in the Cathaysia Block of South China and its tectonic significance. Precambrian Res. 136 (1), 51–66.
Li, X.H., Li, Z.X., Li, W.X., Liu, Y., Yuan, C., Wei, G., Qi, C., 2007. U-Pb zircon, geochemical and Sr–Nd–Hf isotopic constraints on age and origin of Jurassic I– and A–type granites from central Guangdong, SE China: a major igneous event in response to foundering of a subducted flat–slab? Lithos 96, 186–204 (s 1–2).
Li, W.X., Li, X.H., Li, Z.X., 2008a. Middle Neoproterozoic syn–rifting volcanic rocks in Guangfeng, South China: Petrogenesis and tectonic significance. Geol. Mag. 145 (4), 475–489.
Li, W.X., Li, X.H., Li, Z.X., Lou, F.S., 2008b. Obduction–type granites within the NE Jiangxi Ophiolite: Implications for the final amalgamation between the Yangtze and Cathaysia Blocks. Gondwana Res. 13 (3), 288–301.
Li, X.H., Li, W.X., Li, Z.X., Liu, Y., 2008c. 850–790 Ma bimodal volcanic and intrusive rocks in northern Zhejiang, South China: A major episode of continental rift magmatism during the breakup of Rodinia. Lithos 102 (1), 341–357.
Li, Z.X., Bogdanova, S.V., Collins, A.S., Davidson, A., Waele, B.D., Ernst, R.E., Fitzsimons, I.C.W., Fuck, R.A., Gladkochub, D.P., Jacobs, J., 2008d. Assembly, configuration, and break–up history of Rodinia: a synthesis. Precambrian Res. 160 (1–2), 179–210.
Li, X.H., Li, W.X., Li, Z.X., Lo, C.H., Wang, J., Ye, M.F., Yang, Y.H., 2009a. Amalgamation between the Yangtze and Cathaysia blocks in South China: constraints from SHRIMP U-Pb zircon ages, geochemistry and Nd–Hf isotopes of the Shuangxiwu volcanic rocks. Precambrian Res. 174 (1–2), 117–128.
Li, X.H., Liu, Y., Li, Q.L., Guo, C.H., Chamberlain, K.R., 2009b. Precise determination of Phanerozoic zircon Pb/Pb age by multicollector SIMS without external standardization. Geochem. Geophys. Geosyst. 10, Q04010.
Li, Q.L., Li, X.H., Liu, Y., Tang, G.Q., Yang, J.H., Zhu, W.G., 2010a. Precise U-Pb and Pb–Pb dating of Phanerozoic baddeleyite by SIMS with oxygen flooding technique. J. Anal. Atom. Spectrom. 25 (7), 1107–1113.
Li, W.X., Li, X.H., Li, Z.X., 2010b. Ca. 850 Ma bimodal volcanic rocks in Northeastern Jiangxi Province, South China: initial extension during the breakup of Rodinia? Am. J. Sci. 310 (9), 951–980.
Li, X.H., Li, W.X., Li, Q.L., Wang, X.C., Liu, Y., Yang, Y.H., 2010c. Petrogenesis and tectonic significance of the ~850 Ma Gangbian alkaline complex in South China: evidence from in situ zircon U-Pb dating, Hf–O isotopes and whole–rock geochemistry. Lithos 114 (1–2), 1–15.
Li, Z.X., Li, X.H., Wartho, J.A., Clark, C., Li, W.X., Zhang, C.L., Bao, C., 2010d. Magmatic and metamorphic events during the early Paleozoic Wuyi-Yunkai orogeny, southeastern South China: New age constraints and pressure–temperature conditions. Geol. Soc. Am. Bull. 122 (5–6), 772–793.
Lightfoot, P.C., Hawkesworth, C.J., Devey, C.W., Rogers, N.W., Calsteren, P.W.C.V., 1990. Source and differentiation of Deccan Trap Lavas: implications of geochemical and mineral chemical variations. J. Petrol. 31 (5), 1165–1200.
Lindsay, J.F., Brasier, M.D., 2002. Did global tectonics drive early biosphere evolution? Carbon isotope record from 2.6 to 1.9 Ga carbonates of Western Australian basins. Precambrian Res. 114 (1–2), 1–34.
Liu, Y., Liu, H.C., Li, X.H., 1996. Simultaneous precise determination of 40 trace elements in rock samples using ICP–MS. Geochimica 25 (6), 552–558.
Ludwig, K.R., 2003. User's Manual for Isoplot 3.00: A Geochronological Toolkit for Microsoft Excel. Berkeley Geochronology Center (special publication, no. 4).
Melekhova, E., Annen, C., Blundy, J., 2013. Compositional gaps in igneous rock suites controlled by magma system heat and water content. Nat. Geosci. 6 (5), 385–390.
Merle, R., Marzoli, A., Reisberg, L., Bertrand, H., Nemchin, A., Chiaradia, M., Callegaro, S., Jourdan, F., Bellieni, G., Dan, K., 2014. Sr, Nd, Pb and Os isotope systematics of CAMP Tholeiites from Eastern North America (ENA): evidence of a subduction–enriched mantle source. J. Petrol. 55 (1), 133–180.
Millar, I.L., 1999. Neoproterozoic extensional basic magmatism associated with the West Highland granite gneiss in the Moine Supergroup of NW Scotland. J. Geol. Soci. Lond. 156, 1153–1162.
Miyashiro, A., 1974. Volcanic rock series in island arcs and active continental margins. Am. J. Sci. 274 (4), 321–355.
Moores, E.M., 1991. Southwest U. S. East Antarctic (SWEAT) connection: a hypothesis. Geology 19 (5), 425–428.
Murphy, J.B., Dostal, J., 2007. Continental mafic magmatism of different ages in the same terrane: constraints on the evolution of an enriched mantle source. Geology 35 (4), 335–338.
Nance, R.D., Murphy, J.B., Santosh, M., 2014. The supercontinent cycle: a retrospective essay. Gondwana Res. 25 (1), 4–29.
Parman, S.W., Grove, T.L., Kelley, K.A., Plank, T., 2011. Along-arc variations in the pre-eruptive H2O contents of mariana arc magmas inferred from fractionation paths. J. Petrol. 52 (2), 626–636.
Paulsson, O., Andreasson, P.G., 2002. Attempted break–up of Rodinia at 850 Ma: geochronological evidence from the Seve-Kalak Superterrane, Scandinavian Caledonides. J. Geol. Soc. London 159 (11), 751–761.
Pearce, J.A., 1996. A user's guide to basalt discrimination diagram. In: Wyman, D.A. (Ed.), Trace Element Geochemistry of Volcanic Rocks: Applications for Massive Sulphide Exploration, vol. 12. Geological Association of Canada, pp. 79–113. Short Course Notes.
Pearce, J.A., Norry, M.J., 1979. Petrogenetic implications of Ti, Zr, Y, and Nb variations in volcanic rocks. Contrib. Mineral. Petr. 69 (1), 33–47.
Peccerillo, A., Barberio, M.R., Yirgu, G., Ayalew, D., Barbieri, M., Wu, T.W., 2003. Relationships between Mafic and Peralkaline silicic magmatism in continental rift settings: a petrological, geochemical and isotopic study of the gedemsa volcano, Central Ethiopian Rift. J. Petrol. 44 (11), 2003–2032.
Polat, A., Hofmann, A.W., Rosing, M.T., 2002. Boninite–like volcanic rocks in the 3.7–3.8 Ga Isua greenstone belt, West Greenland: geochemical evidence for intra–oceanic subduction zone processes in the early Earth. Chem. Geol. 184 (3), 231–254.
Puffer, J.H., 2001. Contrasting high field strength element contents of continental flood basalts from plume versus. Geology 29, 675–678.
Qiu, Y.M., Gao, S., Mcnaughton, N.J., Groves, D.I., Ling, W., 2000. First evidence of >3.2 Ga continental crust in the Yangtze craton of south China and its implications for Archean crustal evolution and Phanerozoic tectonics. Geology 28 (1), 11.
Saunders, A.D., Tarney, J., 1984. Geochemical characteristics of basaltic volcanism within back–arc basins. Geol. Soc. Lond. Spec. Publ. 16 (1), 59–76.
Shervais, J.W., 1982. Ti–V plots and the petrogenesis of modern and ophiolitic lavas. Earth Planet. Sc. Lett. 59 (1), 101–118.
Shui, T., 1988. Tectonic framework of the continental basement of southeast China. Sci. China (Series B) 31, 885–896.
Sláma, J., Košler, J., Condon, D.J., Crowley, J.L., Gerdes, A., Hanchar, J.M., Horstwood, M.S.A., Morris, G.A., Nasdala, L., Norberg, N., 2008. Plešovice zircon – A new natural reference material for U-Pb and Hf isotopic microanalysis. Chem. Geol. 249 (1–2), 1–35.
Smith, D.J., 2014. Clinopyroxene precursors to amphibole sponge in arc crust. Nat. Commun. 5 (9), 787.
Soper, N.J., Harris, A.L., Strachan, R.A., 1998. Tectonostratigraphy of the Moine Supergroup: a synthesis. J. Geol. Soci., Lond. 155, 13–24.
Stacey, J.S., Kramers, J.D., 1975. Approximation of terrestrial lead isotope evolution by a 2–stage model. Earth Planet. Sc. Lett. 26 (2), 207–221.
Storey, B.C., 1995. The role of mantle plume in continental breakup: case histories from Gondwanaland. Nature 377 (6547), 301–308.
Sun, S.S., Mcdonough, W.F., 1989. Chemical and isotopic systematics of oceanic basalts; implications for mantle composition and processes. Geol. Soc. Lond. Spec. Publ. 42 (1), 313–345.
Suneson, N.H., Lucchitta, I., 1983. Origin of bimodal volcanism, southern Basin and Range province, west–central Arizona. Geol. Soc. Am. Bull. 94 (8), 1005–1019.
Tanaka, T., Togashi, S., Kamioka, H., Amakawa, H., Kagami, H., Hamamoto, T., Yuhara, M., Orihashi, Y., Yoneda, S., Shimizu, H., 2000. JNdi–1: a neodymium isotopic reference in consistency with LaJolla neodymium. Chem. Geol. 168 (168), 279–281.
Taylor, B., Martinez, F., 2003. Back–arc basin basalt systematics. Earth Planet. Sc. Lett. 210 (3–4), 481–497.
Turner, S., Hawkesworth, C., 1995. The nature of the sub–continental mantle: constraints from the major–element composition of continental flood basalts. Chem. Geol. 120 (3–4), 295–314.
Turner, S., Hawkesworth, C., Gallagher, K., Stewart, K., Peate, D., Mantovani, M., 1996. Mantle plumes, flood basalts, and thermal models for melt generation beneath continents: assessment of a conductive heating model and application to the Parana. J. Geophys. Res. 101, 11503–11518.
Wang, X.L., Zhou, J.C., Qiu, J.S., Zhang, W.L., Liu, X.M., Zhang, G.L., 2006. LA–ICP–MS U-Pb zircon geochronology of the Neoproterozoic igneous rocks from Northern Guangxi, South China: implications for tectonic evolution. Precambrian Res. 145 (1–2), 111–130.
Wang, X.C., Li, X.H., Li, W.X., Li, Z.X., 2007. Ca. 825 Ma komatiitic basalts in South China: First evidence for >1500 & #xB0;C mantle melts by a Rodinian mantle plume. Geology 35 (12), 1103–1106.

Wang, X.C., Li, X.H., Li, W.X., Li, Z.X., Liu, Y., Yang, Y.H., Liang, X.R., Tu, X.L., 2008a. The Bikou basalts in the northwestern Yangtze block, South China: Remnants of 820–810 Ma continental flood basalts? Geol. Soc. Am. Bull. 120 (11), 1478–1492.

Wang, X.L., Zhao, G., Zhou, J.C., Liu, Y., Hu, J., 2008b. Geochronology and Hf isotopes of zircon from volcanic rocks of the Shuangqiaoshan Group, South China: implications for the Neoproterozoic tectonic evolution of the eastern Jiangnan orogen. Gondwana Res. 14 (3), 355–367.

Wang, X.C., Li, X.H., Li, W.X., Li, Z.X., 2009. Variable involvements of mantle plumes in the genesis of mid–Neoproterozoic basaltic rocks in South China: a review. Gondwana Res. 15 (3–4), 381–395.

Wang, X.C., Li, X.H., Li, Z.X., Liu, Y., Yang, Y.H., 2010. The Willouran basic province of South Australia: its relation to the Guibei large igneous province in South China and the breakup of Rodinia. Lithos 119 (3), 569–584.

Wang, Y.J., Zhang, A.M., Cawood, P.A., Fan, W.M., Xu, J.F., Zhang, G.W., Zhang, Y.Z., 2013. Geochronological, geochemical and Nd–Hf–Os isotopic fingerprinting of an early Neoproterozoic arc–back–arc system in South China and its accretionary assembly along the margin of Rodinia. Precambrian Res. 231 (5), 343–371.

Wang, X.C., Li, Z.X., Li, J., Pisarevsky, S.A., Wingate, M.T.D., 2014. Genesis of the 1.21 Ga Marnda Moorn large igneous province by plume–lithosphere interaction. Precambrian Res. 241 (1), 85–103.

Wang, X.C., Wilde, S.A., Li, Q.L., Yang, Y.N., 2015. Continental flood basalts derived from the hydrous mantle transition zone. Nat. Commun 6.

Wang, X.C., Wilde, S.A., Xu, B., Pang, C.J., 2016. Origin of arc–like continental basalts: implications for deep–Earth fluid cycling and tectonic discrimination. Lithos 261, 5–45.

Wiedenbeck, M., Alle, P., Corfu, F., Griffin, W.L., Meier, M., Oberli, F., Quadt, A.V., Roddick, J.C., Spiegel, W., 1995. Three natural zircon standards for U-Th-Pb, Lu-Hf, trace element and REE analyses. Geostand. Newslett. 19 (1), 1–23.

Winchester, J.A., Floyd, P.A., 1976. Geochemical magma type discrimination: application to altered and metamorphosed basic igneous rocks. Earth Planet. Sc. Lett. 28 (3), 459–469.

Winchester, J.A., Floyd, P.A., 1977. Geochemical discrimination of different magma series and their differentiation products using immobile elements. Chem. Geol. 20 (4), 325–343.

Ye, M.F., Li, X.H., Li, W.X., Liu, Y., Li, Z.X., 2007. SHRIMP zircon U-Pb geochronological and whole–rock geochemical evidence for an early Neoproterozoic Sibaoan magmatic arc along the southeastern margin of the Yangtze Block. Gondwana Res. 12 (1–2), 144–156.

Zen, E.A., 1986. Aluminum enrichment in silicate melts by fractional crystallization: some mineralogic and petrographic constraints. J. Petrol. 27 (5), 1095–1117.

Zhang, Y.Z., Wang, Y.J., Geng, H.Y., Zhang, Y.H., Fan, W.M., Zhong, H., 2013. Early Neoproterozoic (~850 Ma) back–arc basin in the Central Jiangnan Orogen (Eastern South China): Geochronological and petrogenetic constraints from meta–basalts. Precambrian Res. 231 (231), 325–342.

Zhao, J.H., Zhou, M.F., 2007a. Geochemistry of Neoproterozoic mafic intrusions in the Panzhihua district (Sichuan Province, SW China): Implications for subduction–related metasomatism in the upper mantle. Precambrian Res. 152 (1), 27–47.

Zhao, J.H., Zhou, M.F., 2007b. Neoproterozoic adakitic plutons and arc magmatism along the western margin of the Yangtze Block, South China. J. Geol. 115 (6), 675–689.

Zhou, M.F., Lesher, C.M., 2002a. Neoproterozoic arc–related mafic intrusions along the northern margin of South China: implications for the accretion of Rodinia. J. Geol. 110 (5), 611–618.

Zhou, M.F., Yan, D.P., Kennedy, A.K., Li, Y.Q., Ding, J., 2002b. SHRIMP U-Pb zircon geochronological and geochemical evidence for Neoproterozoic arc–magmatism along the western margin of the Yangtze Block, South China. Earth Planet. Sc. Lett. 196 (1), 51–67.

Zhou, M.F., Ma, Y., Yan, D.P., Xia, X., Zhao, J.H., Sun, M., 2006. The Yanbian Terrane (Southern Sichuan Province, SW China): a Neoproterozoic arc assemblage in the western margin of the Yangtze Block. Precambrian Res. 144 (1–2), 19–38.

Zhou, J.C., Wang, X.L., Qiu, J.S., 2009. Geochronology of Neoproterozoic mafic rocks and sandstones from northeastern Guizhou, South China: Coeval arc magmatism and sedimentation. Precambrian Res. 170 (1), 27–42.

Zhu, G.Q., Chen, Z.J., Yang, S.F., Chen, H.L., 1996. Tectonic characteristics of the Shuangxiwu group and its geological significance in northern Zhejiang province. Geol. J. Univ. 2 (1), 58–64.